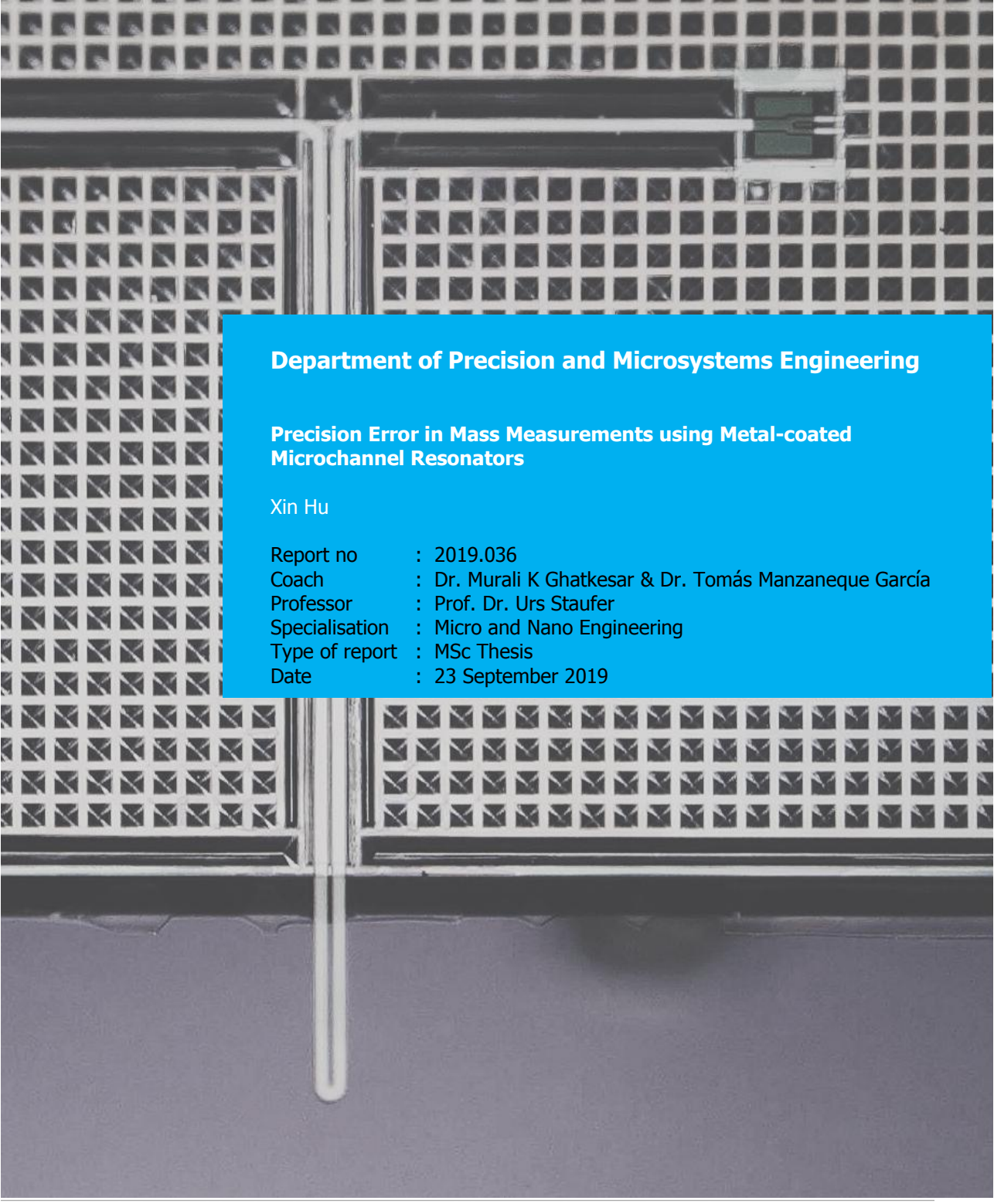

Department of Precision and Microsystems Engineering

Precision Error in Mass Measurements using Metal-coated Microchannel Resonators

Xin Hu

Report no	:	2019.036
Coach	:	Dr. Murali K Ghatkesar & Dr. Tomás Manzaneque García
Professor	:	Prof. Dr. Urs Staufer
Specialisation	:	Micro and Nano Engineering
Type of report	:	MSc Thesis
Date	:	23 September 2019

TU Delft Delft University of Technology

Challenge the future

Precision Error in Mass Measurements using Metal-coated Microchannel Resonators

by

Xin Hu

For the degree of Master of Science in Mechanical Engineering
at Delft University of Technology,

submitted on Sunday 22 September 2019.

Student number: 4677692

Thesis committee: Prof. Dr. Urs Staufer (Chair)
Dr. Murali K Ghatkesar (Supervisor)
Dr. Tomás Manzaneque García (co-supervisor)
Dr. Richard Norte (external examiner)

An electronic version of this thesis is available at
http://repository.tudelft.nl/.
The thesis is on embargo till 31 Dec 2020.


TU Delft
Delft
University of
Technology

Abstract

A resonator is a device or system that exhibits resonance or resonant behavior. That is, it naturally oscillates with greater amplitude at some frequencies, called resonance frequencies, than at other frequencies. It is prevalent in the domain of precision mass measurements thanks to the high sensitivity of its dynamic characteristics to mass changes. A microresonator is a miniaturized resonator that is typically working in liquid to facilitate the mass measurements of micrometer-scale biological and chemical specimens. However, the liquid environment severely degrades its quality factor and limits the mass precision.

The design of suspended microchannel resonators has been a solution. By constraining the liquid inside an embedded microchannel, the device can be installed in vacuum to get rid of viscous damping. But the lack of heat transfer in vacuum means heat accumulation inside the device, especially when it is measured by a laser doppler vibrometer. This brings instability to the dynamic performance through thermoelastic coupling, and introduces errors in mass measurements. This has become one of the main obstructs for a finer mass precision.

This work aims at determining such instability and its relation with other parameters, such as the thickness of the metal coating on the surface of the microresonator, and the position on the microresonator whose vibration is sensed with a laser beam. Three eigenmodes of the device are studied: the first and second flexural modes, and the first torsional mode.

My tasks include characterizing the microresonator in different vacuum levels, doing continuous modal measurements on one microresonator before and after a layer of Au/Pd coating is applied onto its top surface, and testing other two water-filled microresonators to look into their performance with liquid.

It is concluded that the presence of Au/Pd coating actually leads to a poorer stability and larger mass error. The same holds for higher eigenmodes compared to the fundamental eigenmode. Moreover, the water filling helps to increase the quality factor and decrease the mass error in our case.

Contents

List of Figures

List of Tables

Acknowledgement

This thesis is made as a completion of the MSc Mechanical Engineering at Hi-Tech Engineering (HTE) in TU Delft. It is accomplished under the cooperation with many people. Hereby I would like to thank you all for your direct and indirect contribution to this thesis. Without your efforts, this accomplishment would not be possible.

Dear Murali Krishna Ghatkesar, thank you for being my supervisor. It is a great pleasure to have the weekly meeting with you. You are always able to break the frame and think from new aspects, which gave me great inspiration. You also showed me the charming wisdom of scientific research, and reminded me to keep my motivation whatever I do.

Dear Tomás Manzaneque García, thank you for being my daily supervisor. You have accompanied me throughout the whole project, not only teaching me basic theories, but also giving me lots of guidance in the lab. Your broad knowledge, proficient skills and earnest attitude have left deep impression on me. It is so pleasant to work with you.

Dear Pierpaolo Belardinelli, thank you for bringing me to this project with your passionate lab introduction. Also, thanks for sending me beautiful codes and useful suggestions on the use of the VNA.

Dear Ivan Buijnsters, Saleh Aghajani, Rob Luttjeboer, Patrick van Holst and Gideon Emmaneel, thank you all for the lab training and instructions you provided to me.

Dear Arun Gunda, Nimit Kothari and Alok Bharadwaj, thank you all for your help and accompany in the lab. Hope we could work together again in the future.

Dear Xiaojun Hou and Chengwei Cai, thank you for your advice on all kinds of affairs. Dear Chuqian Zhang and Yi Song, thank you for your comfort when I felt stressed. And to all my friends and colleagues, thank you for your encouragement to me. It gave me much power to face the challenges. Wish you all the best in the future.

Finally, my dear family, thank you for your support and trust in me during these two years of study. I love you, and I hope one day you can be proud of me.

Xin Hu
Delft, September 2019

1

Introduction

Micro-cantilevers, with their simple structure, miniaturized dimensions and great versatility, are widely applied in micro and nano-engineering. One typical application is the probe on atomic force microscopy (AFM), which can measure the topology of a surface with atomic resolution. Integrated with other sensors, cantilevers also serve as an ideal measurement tool in a variety of fields.

One technique which exploits the intrinsic characteristic of cantilevers is mass measurement based on resonance frequency. The resonance frequency of a cantilever is simultaneously determined by both its effective mass and stiffness. When the effective mass changes, the shift in the resonance frequency reveals information about the amount of added mass. The adsorption of specific kinds of particles can be achieved, thanks to the functionalization of the surface of the cantilever.

Such functionalized cantilevers, called micro or nano-resonators, provide a decent method for mass measurement. In order to correct their poor adaptation to aqueous environments, a new design in the structure was proposed, allowing the particle-carry liquid to flow through the interior of a cantilever. These new micro-resonators, known as suspended micro-channel resonators (SMR), present a great improvement in performance, proving to be one of the most reliable mass measurement techniques in micro scale.

As SMRs are usually enclosed in a vacuum chamber to refine their sensitivity and resolution to the fullest, the lack of heat dissipation induces an extra challenge to study how the heat brought in by the vibration-detecting optical device and absorbed by the SMR will affect its dynamic characteristics. Although several studies have been focused on thermoelastic

effects on cantilevers, they are neither comprehensive nor accurate, as few of them focused on factors other than the intensity and position of the detecting laser, and none is directly targeted for SMR. In this project, the contribution of other important parameters to the thermoelastic coupling effects of SMR will be studied, and an optimal condition which consists of a combined set of different parameters will be summarized.

1.1. Applications of Micro-cantilevers

A micro-cantilever is a beam in micron-level dimension, with one end anchored to a fixed base and the other end free to vibrate. It can be fabricated readily from silicon, silicon dioxide, silicon nitride or other materials in large batches. It finds its wide application especially in biology, pharmaceutics and chemistry industry.

1.1.1. Atomic force microscope

Atomic force microscopy (AFM) is one of the most important tools for operation, measurement and imaging in nano-scale. The core part of an AFM is a micro-cantilever probe with an apex of atomic dimension (in order of magnitude of 10^{-10} m). It measures the force between the atoms on the probe and the atoms on the sample, and thus creates an overview of the 3D topology of the sample. It can work on both conductors and insulators, and in both contact and non-contact modes, which ensures its advantage in its versatility over other atomic microscopes, such scanning tunneling microscope (STM).

1.1.2. Electrical conductor

Researchers have reported a method to fabricate a conductive single-wall carbon nanotubes (SWNT) on the terminus of a cantilever (see Figure 1.1), so that the cantilever is able to generate electric field to locally oxide a metal, to create nanostructures [17] or store data at a high density. [1]

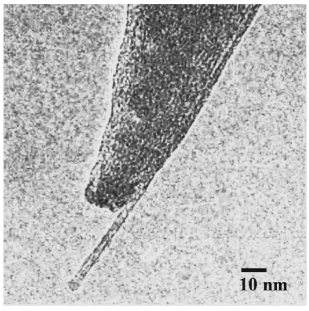

Figure 1.1: SWNT synthesized at the tip of a silicon cantilever [1]

1.1.3. Particle sensors

In micro-sensing regime, especially the sensing of chemical and biological substances, label-free methods are preferable over labelled methods because of its shorter processing period and less interference on the reactants [18]. Basically, the physical properties of cells or particles are detected in label-free sensing, such as mass, surface stress, surface potential or charge, refractive index, etc. These parameters can be read out directly, providing a simple-handling assay method.

When integrated with micro-fabricated sensors at its end, cantilevers serve as a decent tool in label-free detection. With the capability of real-time, multiplexed, label-free sensing with extremely low volume of sample needed [19], cantilevers are used in a wide range of micro-sensing systems.

In some cases the cantilever itself needs surface functionalization with receptor molecules exquisitely sensitive to bind with target chemical or biological molecules, so as to facilitate the immobilization of them.

Static mass and stress sensing

In early studies, one side of the cantilever, usually the bottom side, was functionalized with receptor molecules that only bind with a certain kind of target molecules. When the cantilever was immersed into a carrier liquid, the target molecules in the liquid were adsorbed to the receptors, bringing an additional mass as well as an induced stress due to the interaction between the absorbed molecules, which bends the cantilever. By detecting the deflection of cantilever, the existence of that specific kind of target molecules could be ascertained. This technique has been demonstrated for detecting protein molecules as an early diagnosis, such as detecting IgE with DNA aptamer as the receptor [20].

Dynamic mass sensing

The immobilization of extra mass depicted above also induces change in the dynamic characteristic of the cantilever. The expression of the fundamental resonance frequency of a cantilever, f_0, is derived from the equation of motion of a Bernoulli–Euler beam, and depends on the effective mass m_{eff} and stiffness k of the cantilever (see Equation 1.1).

$$f_0 = \frac{1}{2\pi}\sqrt{\frac{k}{m_{eff}}} \tag{1.1}$$

While the immobilized molecules add to the total mass which vibrates, a shift in the resonance frequency of the structure will be observed, giving a quantitative insight to the additional mass. This is the basic principle of the micro-resonators that will be discussed in the next section.

1

Surface charge and potential sensing

When charged molecules hybridize onto the functionalized surface of a cantilever, an increase in surface charge on the cantilever will be induced. Using micro-fabricated field-effect sensors, the real-time surface charge can be detected, so that the immobilization of the target molecules will be sensed directly. J. Fritz *et al.* [2] reported such a method to electronically detect DNA by its intrinsic molecular charge. In their research, probe DNA molecules are bound electrostatically on the cantilever, facilitating the immobilization of their complementary DNA counterparts (See Figure 1.2).

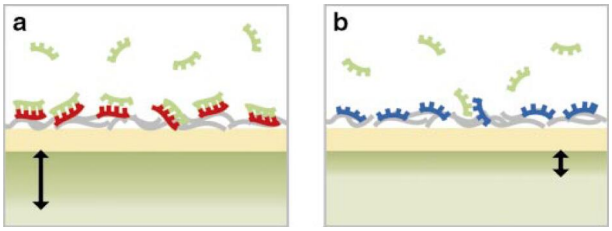

Figure 1.2: Complementary receptor-ligand pairs (red and green ones in the left) and non-complementary DNAs (blue and green ones in the right) [2]

*p*H sensing

Cantilevers integrated with micro-fabricated field-effect sensors are also applied in sensing *p*H of liquids. Because of its high sensitivity and miniaturized size, the hybrid device is able to sense the *p*H gradient across a multi-layer laminar flow formed by a series of fluid flows of different *p*H, with very little amount of sample needed [21].

1.1.4. Interdigitated finger design

One method to eliminate environment disturbances, such as transient variation in temperature, pressure or even refraction index in aqueous environment, is by using interdigitated fingers (ID fingers) to detect the differential deflection of two cantilevers which constitute a sensor-reference pair, as shown in Figure 1.3. In this way, the resolution of deflection sensing can be improved to 3×10^{-13} m [22], and the noise is reported to be reduced by up to 50 times compared to absolute deflection sensing in low frequency range [23]. Since this concept was first put forward by C. Savran *et al.* [20], ID finger structures have been adopted in a variety of early cantilever-based sensors, such as mass sensors, accelerometers [24] and Boltzman's constant [3].

1.2. Micro and Nano-resonators

As introduced in the last section, micro-resonators, designed for mass sensing, are basically cantilevers working in their dynamic mode. In addition, researchers have used single-wall

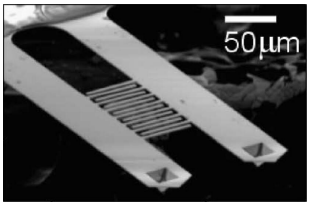

Figure 1.3: Image of a group of interdigitated fingers between two cantilevers [3]

carbon nanotubes (SWNT) as nano-resonators, showing better sensitivity than conventional micro-resonator.

1.2.1. Sensitivity

The expression of the sensitivity to mass changes of a micro-resonator can be derived from Equation 1.1, see Equation 1.2.

$$\frac{\delta f}{\delta m_{eff}} = -\frac{1}{2}\frac{f}{m_{eff}} \tag{1.2}$$

Therefore, the sensitivity, defined as the change in resonance frequency corresponding to a unit change in mass, is proportional to the absolute value of the resonance frequency, and inversely proportional to the effective mass of the vibrating body. It reveals two ways as to improve the sensitivity - reducing the vibrating mass by miniaturization, and looking into higher order of resonance with higher eigenfrequency.

1.2.2. Resolution

From Equation 1.2, the mass resolution, e.g. the minimum mass change that the device is able to detect, is expressed in Equation 1.3.

$$\delta m_{eff} = -\frac{2m_{eff}}{f}\delta f \tag{1.3}$$

In addition to the effective mass and resonance frequency, the frequency resolution also contributes to the mass resolution. Therefore, apart from the methods mentioned above, improving the frequency measuring device so that smaller frequency shift could be detected is another effective means to improve the resolution of the whole mass-sensing resonator.

1.2.3. Nano-resonators

In comparison with micro-resonators, nano-resonators are resonators miniaturized down to the nano-scale. With their extremely miniaturized dimensions, they can achieve a much higher resonance frequency, which is greatly beneficial for improving mass sensitivity and

resolution in detection. Moreover, it opens a gate to the tracking of quantum imprint directly [25].

Nano-resonators based on carbon nanotubes (Figure 1.4) work in the GHz range, and their resolution is usually below zeptogram (10^{-21} g) level. J. Chaste *et al.* reported a mass sensing experiment whose resolution reached an astonishing 1.7 yg (yoctogram, 10^{-24} g), equivalent to the mass of a single proton [4].

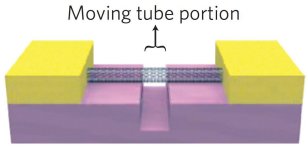

Figure 1.4: Structure of one of the carbon nanotube resonators [4]

1.3. Development of Suspended Microchannel Resonator

A suspended microchannel resonator (SMR) is a micro-cantilever with a micro-channel embedded in its interior. As for other micro-resonators, the resonance frequency shift of SMR is a characterization of its mass change due to flowing through substances or surface-adsorbed particles.

Commercialized SMR have evolved into different forms, including resonating U-tubes and suspended resonator plates. Taking advantage of transparent materials like silicon dioxide, direct visual inspection for the fluid in the channel is made possible [8]. Nowadays, SMR have been extensively used for sensing mass, density, viscosity and other fluid or particle properties in chemical and pharmacy.

1.3.1. Motivation for the design of SMR

Conventional micro-resonators are designed for the sensing of chemical and biological molecules and even living cells for which liquid environment is necessary to keep them active. Traditionally, the whole resonator is immersed into the sample liquid where the target species to be immobilized onto the resonator are present. However, since a resonator works in dynamic mode, the great damping and extra effective mass introduced by the surrounding liquid poses an immediate adverse effect to its performance.

The quality factor (Q) is a characterization of the energy loss within a mechanism. It is defined by the ratio of the energy stored in the resonator to the energy dissipated per cycle. There are some other explanations to Q which are suitable to describe a resonator, among which R. Datar *et al.* [26] explains it as a ratio between the resonance frequency and the width of the frequency spectrum at half the maximum amplitude.

As a resonator vibrates in liquid, the strong viscous drag between the resonator and liquid produces high damping which enhances the energy dissipation mechanism and degrades the quality factor. In such scenario, vibration dies out quickly, so the accuracy of sensing cannot

be guaranteed. Also, an extra effective mass due to surrounding liquid vibrating along with the resonator further damages its sensitivity.

In order to get rid of the viscous damping, researchers suggested a 'dip and dry' method [27]. During the 'dip' stage, target species are immobilized onto the resonator while it is dipped in liquid. Afterwards, the resonator is dried, and its resonance frequency is measured with target species still attached on it, and compared to its original frequency. The drawbacks of long period and possible property alternation of the species after being dried make it highly inefficient. Later, T. Burg *et al.* [5] introduced a different approach by putting the liquid inside the resonator. With a U-shaped microchannel fabricated inside a cantilever, fluid is allowed to flow into the cantilever from a reservoir, and flow back into a reservoir again, forming a circulation, as shown in Figure 1.5. Furthermore, the microchannel resonator is packaged into a vaccum chamber, so that the viscous drag of air, is removed entirely. This design effectively avoids the degradation of quality factor brought by a surrounding aqueous environment, reaching a quality factor of ~15,000 even with liquid filling inside. This is 100-fold better than conventional micro-resonator. Meanwhile, it still allows the interaction on the interface between fluid and resonator. Since the fluid is entirely confined to the interior of the resonator, its volume is controllable, which means its density can be derived by measuring its mass that vibrates together with the resonator. Moreover, compared to a large liquid sink, only little volume of sample liquid is needed to fill in the microchannel, which is more economical and more feasible when it comes to testing body liquid. Finally, customized design on the microchannel opens up the possibility to explore some other properties of molecules and cells.

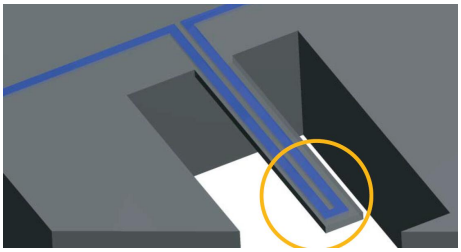

Figure 1.5: Illustration of an SMR [5]

1.3.2. Working principle of mass measurement

As introduced before, the function of SMR relies on the resonance frequency shift due to additional mass. However, the position where mass is added also play an important role in the amount of frequency shift. The governing expression describing the resonance frequency of an SMR is given by Equation 1.4 [28]:

$$f = \frac{1}{2\pi}\sqrt{\frac{k}{m^* + \alpha \triangle m}} \tag{1.4}$$

where m^* is the mass of the resonator itself, Δm is the added mass, and α is a parameter related to the distribution of the added mass relative to the dimension of the resonator. Theoretically, α varies from 0 to 1 when an added point mass moves from the clamping base to the end of the resonator, but calibration of its value for each resonator under uniform mass distribution is required in practice. This is usually done by flowing a liquid of known density through it, such as a glycerol solution.

SMR can be used for sensing the mass of flowing-through liquid or a particle in the carrier liquid. For a liquid, its mass is supposed to uniformly distribute along the microchannel, and is possible to calculate with a calibrated α. It is different when it comes to a particle, because its added mass, compared to the situation where no particle is contained in the carrier liquid, equals to the mass of the particle subtracting the mass of liquid it replaces by its volume, or its 'buoyant mass'. Therefore, only by repeating the experiment using carrier liquids of different densities and interpolating the results could the mass of the particle be known.

Currently, the resonance frequency of an SMR can be measured in a few parts per 10^9, yielding a mass resolution in femtogram (10^{-18} kg) level with only picoliters (10^{-12} L) of sample needed [29]. Specifically, a resolution of about 50 fg for a live single cell was achieved by Stevens *et al.* [30].

1.3.3. Vibration detection methods

One important issue in the application of micro-resonators is frequency detection, which virtually boils down to the continuous detection of the deflection of the resonator. There are basically two methods to detect the deflection: optical and electromechanical.

Optical detection exploits a beam of laser which is focused onto the resonator. Three modes are widely used: optical lever where the shift of laser beam represents the deflection of resonator, interferometry where the interference pattern of two laser paths reveals how much the resonator deflects, and Doppler-effect based vibrometry where the instantaneous velocity of the resonator could be extracted from the frequency difference between the incident and reflected light beams. The main challenge in optical detection is the thermoelastic coupling effect induced by the heat that is introduced by the laser beam and finds no way to dissipate except for conduction to the clamping base along the resonator in vacuum environment.

Without surrounding liquid, the installation of electromechanical sensors on the surface of the SMR is also made possible. J. Lee *et al.* [31] and A. Pastina *et al.* [32] demonstrated the use of piezoresistive sensors fabricated into the SMR and connected to a control circuit.

1.3.4. Continuous mass tracking

Different from transient mass sensing which only measures the passing-through liquids or particles in a short time, trapping of a single cell inside the SMR allows for long-term tracking of its mass, and investigating the mass accumulation rate (MAR) [6]. MAR is a measurement of cell growth without proliferation, and is related to the characteristics of a cell in a couple of aspects - natural growth and agglomeration [11], therapeutic susceptibility

[33], response to osmotic shock [28] - to give some examples. Several trapping techniques have been discussed in literature, including external electric field [34], centrifugal force (Figure 1.6), structural constraint, etc.

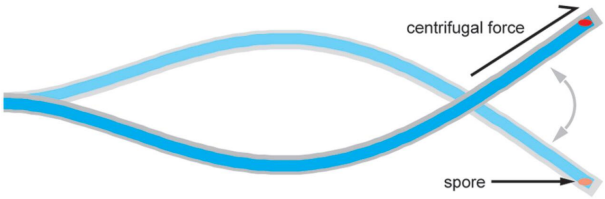

Figure 1.6: Centrifugal trapping of a spore at the end of a SMR [6]

1.3.5. Other applications of SMR

By sensing real-time mass change, SMR is reported as an alternative for particle counting [35].

Apart from mass sensing, SMR also finds its application in determining the density, volume, deformability [9] and electrophoretic mobility [10] of particles and cells, as well as density and viscosity of liquid samples.

SMR can be integrated with upstream and downstream stages, such as liquid preperation and sample separation, into a lab-on-chip or miniaturized total analysis system (μ-TAS), therefore reducing workload and improving throughput.

Density measurements

Measuring the density of a liquid is relatively simple, by dividing its mass obtained using SMR by its volume that is regarded equal to the volume of the microchannel inside SMR.

The density of a particle, like its mass, could not be directly measured. In fact, the buoyant mass of a particle is in linear relation with the density of carrier liquid. Measuring the frequency shifts with the sample passing through the channel in at least two carrier liquids of different densities and interpolating the results yield the average density of the group of samples [36]. As shown in Figure 1.7, the buoyant mass of a single cell measured in two kinds of carrier liquids is represented by the red dots, and the intercept point of the interpolation line with the x-axis represents the density of the fluid in which the buoyant of the cell is zero, i.e. cell density matches fluid density. As a result, this fluid density is exactly the density of the cell.

However, in order to obtain the interpolation line, at least two data points should be acquired separately. Therefore, either repeatability error and error by cross contamination of different liquids when only one SMR is used or instrumental error when multiple SMRs are used will be introduced. Bryan *et al.* [7] designed a novel dual SMR where two resonators are connected by a fluid channel (see Figure 1.8), making two different kinds of liquid run through the device simultaneously, thus enabling the density measurement by once.

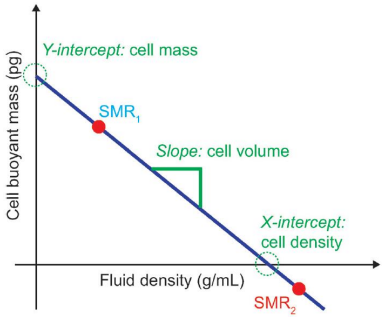

Figure 1.7: Interpolation of buoyant mass in two liquids for density measurement [7]

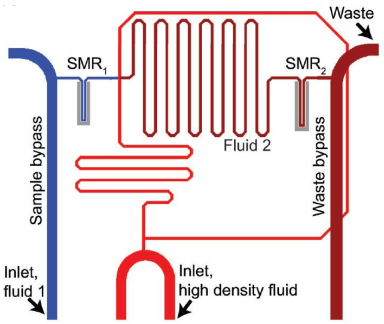

Figure 1.8: Schematic of dual SMR for density measurement [7]

The performance of SMR in density measurement outweighs other density measuring techniques. Son *et al.* [37] reported that the resolution of particle density can reach as high as 0.03%. For liquid density, Khan *et al.* [8] achieved a resolution of 0.01kg/m^3 and a sensitivity of 16Hz/(kg/m^3) respectively.

Viscosity measurements

M. Khan *et al.* [8] presented a method to measure the viscosity of a fluid with SMR. They found that the ratio between the viscous damping coefficients of a filling fluid and an empty SMR is linearly dependent on the viscosity of the fluid, with an accuracy of 0.025 mPa·s. However, it only applies when the viscosity is varying within a very narrow range (see Figure 1.9).

Deformability measurements

The deformability is a characteristic used in early recognition of the type of a cell, such as distinguish between tumor cells and blood cells. S. Byun *et al.* [38] designed a constriction into the microchannel within SMR to squeeze cells with the help of flushing liquid (see Figure 1.10 for example). The time a cell spends in passing the constriction is related to

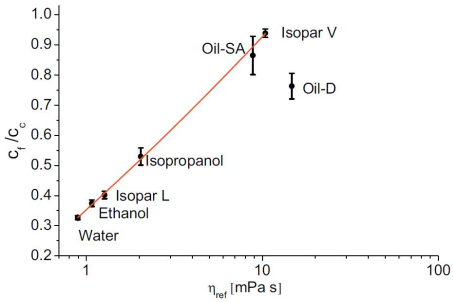

Figure 1.9: Linear dependence of the ratio between viscous damping coefficients on the viscosity of a fluid [8]

its deformability - better deformability, less friction with the constriction walls, and shorter passage time.

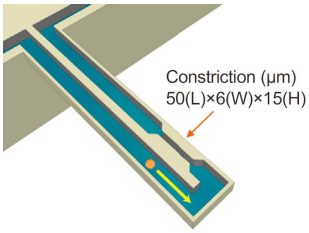

Figure 1.10: Schematic of an SMR with a constriction [9]

As mentioned before, the resonance frequency shift of SMR is sensitive to the position of the added mass. As cells move slowly through the constriction, it offers an opportunity to observe the frequency-position response of the device. J. Shaw Bagnall *et al.* [39] further found a correlation between the shape of peak in the time-varying frequency curve and the cell type, which indicates another way in the early recognition and classification of cells.

Electrophoretic mobility measurement

Electrophoretic mobility is another particle property that could be extracted from the frequency-position dependence. When a periodic electric field is applied across the inlet and outlet of the microchannel, the particle inside will oscillate under a combined effect of electrophoresis and electroosmotic flow, showing a ragged frequency-time curve (see Figure 1.11) that can be analyzed to determine the electrophoretic mobility of the discrete particle [10].

1.3.6. Error control

Temperature change of SMR affects both its vibration characteristic through thermoelastic coupling and the vitality of the chemical or biological substance being detected which also survives certain temperature range, especially the temperature variation induced by the detecting laser beam when the device is in vacuum. Cermak *et al.* [40] and Lee *et al.* [31]

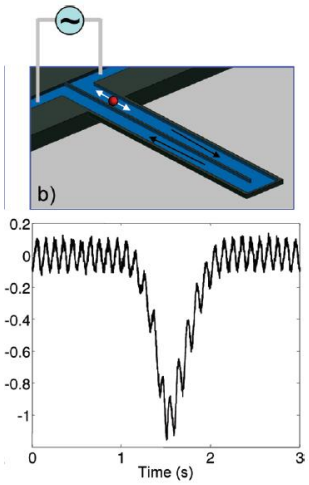

Figure 1.11: Schematic of applying electric field on SMR (up) and the frequency curve with electrophoretic response [10]

introduced the use of the piezoresistive detection method in order to get rid of the laser. Other researchers attempted to directly control the temperature of SMR by placing it on a heat sink connected to a water circulator which adjusts the temperature quickly via a thermoelectric module and maintains the temperature of the device constant at the optimum value for the specific species throughout the whole process of measurement [29]. The effect of thermoelastic coupling is discussed in detail in the next section.

Another source of error is dependent on the lateral position variation of the detected particle inside the microchannel, called position-dependent error. While the width of the channel is usually much larger than the particles, it allows them to wander in the direction orthogonal to the flowing direction along the resonator, creating an 8% error in an 8μm-wide channel when the particle travels along the outer sidewall instead of following the centerline of the channel [5]. Position-dependent error could be significantly controlled by hydrodynamic focusing, better microchannel design, or measuring the resonance frequency of a higher eigenmode from its antinode [37]. Compared with uncontrolled data, the root-mean-square error of measured frequency is reported to have a 5-fold decrease with hydrodynamic focusing that confined the particle on the centerline of the channel, and a 31-fold decrease when the resonance frequency of the second vibrational mode is measured from the antinode, as shown in Figure 1.12.

1.3.7. Suspended nanochannel resonator

A path to improve the sensitivity and resolution of a resonator is reducing its mass by miniaturization. The application of this principle is the suspended nanochannel resonator (SNR), whose dimensions are typically one-fifth to one-tenth of the dimension of an SMR. This leads to a more than 100-fold decrease in mass, and a 100-fold improvement in resolution

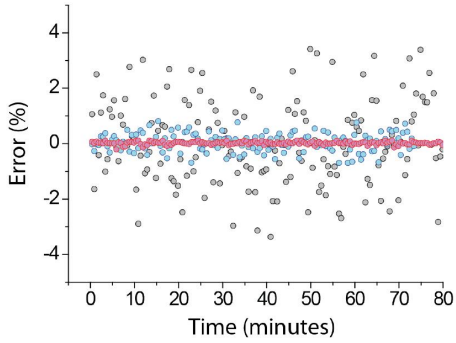

Figure 1.12: Comparison of errors in resonance frequency measured from uncontrolled device (grey dots), under hydrodynamic focusing (blue dots) and from the second eigenmode (pink dots). Data are sampled twice per minute, each time with one single identical cell traveling through the channel [11]

as well. A mass resolution of 27 ag (attogram, 10^{-21} kg) on SNR has been demonstrated by J. Lee *et al.* [41], with no significant drop in quality factor. As a side effect, the manufacturing complexity increases dramatically as the dimension goes down.

1.4. Thermoelastic Coupling Effect on SMR

Since optical detection method finds its prevalent application in recording the vibration of commercial micro- and nano-resonators [42], there have been proofs stating that the detecting laser beam heats the cantilevers to a considerable extent [43], especially in the scenario where a rather strong optical input is required in order to increase the signal-to-noise ratio and thus obtaining higher precision [44]. This temperature variation on the device is the source of its mechanical property changes in many regards, which significantly weakens its reliability. The situation is made even worse by packaging the whole device into a vacuum chamber, where, without the presence of large amount of liquid as heat transfer media, the heat introduced by the detecting laser could only be dissipated via conduction along the cantilever to the clamping base. In recent years, an increasing number of studies have looked into this ”detection induced error”, and have revealed a couple of aspects of the highly interconnected thermoelastic coupling network.

1.4.1. Stiffness vs. resonance frequency

As discussed in Section I, the resonance frequency of a cantilever is simply related to its stiffness and mass (Equation 1.1). As the mass of a cantilever is seen as constant throughout the vibration process, it is wise to focus our eyes on the only variable, stiffness, which makes the problem simpler - the resonance frequency is positively correlated to the stiffness of a cantilever. And the effect of stiffness could be further decoupled into three sources of contribution - change in Young’s modulus, change in geometry, and induced stress [45].

1.4.2. Young's modulus and geometry vs. stiffness

The stiffness of a solid cantilever (without hollow channel) is given by

$$k = \frac{3EI}{l^3} \tag{1.5}$$

Here, two aspects are involved, i.e. the Young's modulus of its material E, and the geometry of the cantilever (the moment of inertia, I, is determined by the width and height of the cantilever, while the length appears directly in the equation). As a result, a reasonable analogy could be made to infer that the material's Young's modulus and the geometry of a hollow cantilever are the factors that directly affect its stiffness.

1.4.3. Stress vs. stiffness

Another factor that is decisive to the virtual stiffness of a structure is the internal stress induced either by an external load or by the structure's geometry change. R. Karabalin *et al.* tested the frequency shift happening on three cantilevers of different lengths on which surface stress was applied (see Figure 1.13) [12]. It is proved that surface stresses incur shifts in resonance frequency due to the change of the structure's stiffness. Michael J. Lachut *et al.* [46] reported the same phenomenon on cantilever plates from a theoretical perspective, and this effect of surface stress on stiffness can be generalized onto any suspended structure.

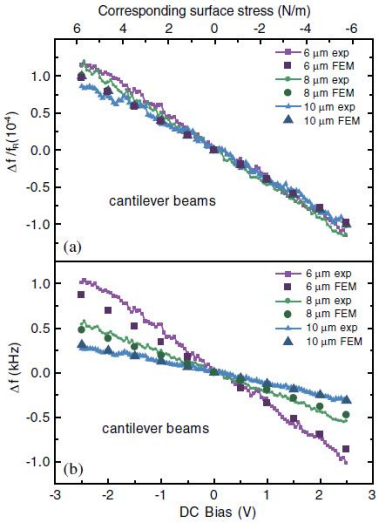

Figure 1.13: Experiment and FEM results of resonance frequency shift on three cantilevers under surface stresses: (a) relative frequency shift and (b) absolute frequency shift [12]

1.4.4. Temperature vs. geometry and geometry vs. induced stress

Thermal expansion is one of the most fundamental physical properties of materials. Typically, the scale of linear expansion of a given material under certain temperature is defined by its thermal expansion coefficient

$$\alpha_L = \frac{1}{L}\frac{\mathrm{d}L}{\mathrm{d}T} \tag{1.6}$$

which denotes that a mono-material object is supposed to expand isotropically under a uniform temperature field. However in the case of SMR, due to the huge amount of heat brought in by the detecting laser beam and the poor heat dissipation effect of conduction process, the time span during which the optical detection is operated is far from enough for a steady and uniform temperature field to evolve. Therefore, the thermal expansion of an SMR is found to be highly anisotropic and non-linear, which eventually induces stresses attempting to pulling the irregular geometry back to its origin shape.

1.4.5. Temperature vs. Young's modulus

Like thermal expansion, Young's modulus is also dependent on temperature. Researches have shown that the temperature dependence of Young's modulus varies greatly from one material to another, even between an elementary substance and its compounds, such as Si and SiO_2, two common materials of which SMRs are made [13][47] (see Figure 1.14).

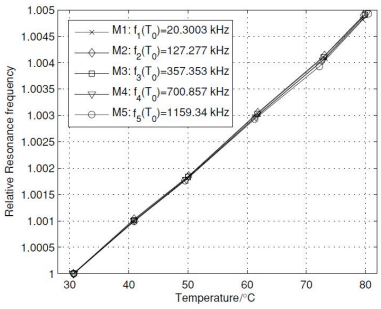

Figure 1.14: Measurement on the relative resonance frequency of the first five flexural modes with respect to uniform temperature variation from R. Sandberg *et al.*. The linear function of temperature is in well accordance with the temperature dependence of Young's modulus of silicon dioxide [13]

1.4.6. Influence of coating

Different from pure silicon or silicon dioxide cantilevers, a coated SMR has different thermal expansion coefficients and Young's moduli in different layers of its bi-material structure, and presents different performances under the same varying temperature field [14], contributing to the stiffness change and frequency shift, especially with larger coating thickness and area [48]. J. Mertens *et al.* gave a decent explanation of this phenomenon on cantilevers. With

the presence of coating, the frequency response to temperature change is no longer linear as in the mono-material case, but displays a rising non-linearity with the increase of coating thickness, because the difference in the thermal expansion between the cantilever body and the coating induces large stress between the two materials (see Figure 1.15). In addition, frequency instability has also been observed on coated SMR.

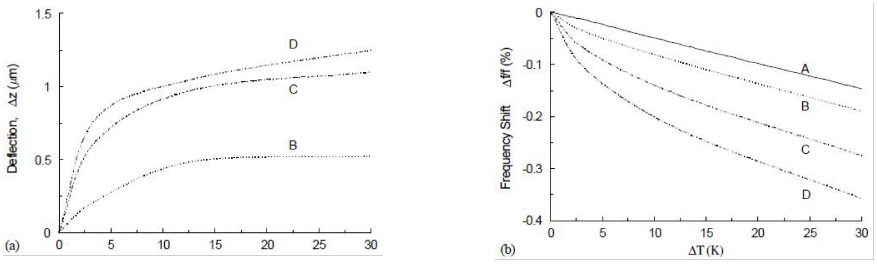

(a) (b)

Figure 1.15: One uncoated cantilever (A) and three coated cantilevers with increasing coating thickness (B-D) were tested under same uniform temperature rise. (a) Within the elastic deformation regime of the coating material, cantilevers with thicker coating showed larger deflections because of larger stresses were induced by larger differential thermal expansion, while the uncoated cantilever did not deflect at all. As temperature kept rising, the induced stress exceeded the fatigue strength of the coating material, the differential thermal expansion stopped growing up, so no more stress was induced, and the cantilever ceased to deflect any further. (b) In scenarios where the induced stress remained unchanged, the frequency response to temperature rise is linear, which can be explained by the sole effect of changing Young's modulus. While the induced stress was changing, the non-linearity in frequency-temperature function is the consequence of a compound effect of variations in both Young's modulus and stress. This study is also a nice example showing the relation between stress and stiffness [14]

There is a more complex interaction between the detecting laser and the coating of SMR in the regard of temperature change. Metal coatings, with better reflectivity and thermal conductivity than silicon or silicon compound, help in reflecting laser power and conducting the heat. This reduces the power absorbed by the structure and promotes the heat dissipation process, mitigating the temperature change happening on it. In the meantime, a larger amount of laser power is reflected back to the sensor, giving a stronger and more recognizable signal over background noise. Therefore, the lower limit of detectable signal is improved. However, the larger specific heat of metal materials than silicon or materials means that the temperature of coated samples rises higher than uncoated ones under the same conditions, which counteracts with the benefits mentioned above. It is only by experiments that it can be made clear if the effect of a specific type of coating on the temperature change is positive or negative.

Overall, which material is the most suitable for the coating material, in terms of its reflectivity, specific heat, thermal conductivity, thermal expansion and compatibility for fabrication, is highly worth studying.

1.4.7. Laser power vs. temperature

The intensity of detecting laser beam is closely related to the temperature of SMR. Since a considerable amount of incident laser power is absorbed by the device, its temperature will inevitably rise. As instinctive as it is, and as proven by theory and experiment [15], more intense laser power can bring about higher temperature (see Figure 1.16 and Figure 1.17).

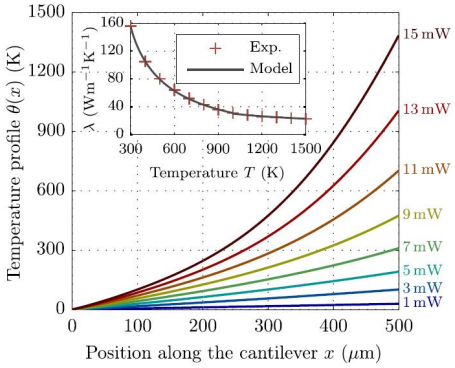

Figure 1.16: Theoretical analysis of temperature profiles along a cantilever with lasers of different intensities being focused at its end [15]

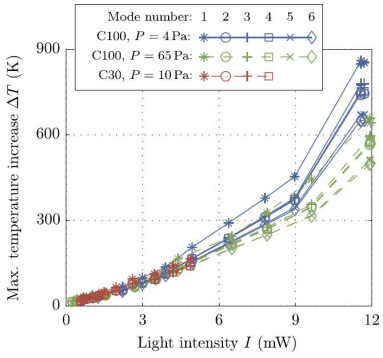

Figure 1.17: Prediction of maximum temperature rise of cantilevers from their performances in different modes, as a function of laser intensity [15]

1.4.8. Laser position vs. temperature

In practice, the detecting laser is not always focused at a single point on SMR, but a group of evenly distributed points (usually 20-30) are selected to generate the average frequency spectrum and mode shape. When the laser moves along the device, the temperature profile changes therewith, as the highest temperature is always at the incident point, and gradually lowers down from the incident point to the base. B. Bircher *et al.* [16] reported different

1

deflections of a cantilever as a characterization of its temperature when a laser beam strikes different points on it (see Figure 1.18).

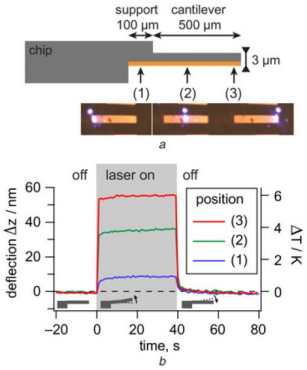

Figure 1.18: Deflection and temperature rise of a cantilever with respect to the laser position [16]

1.4.9. Coupling between temperature profile and mode shape

As a non-uniform temperature distribution affects the materials' Young's moduli and induces stress - both are responsible for the stiffness variation, the mechanism behind this highly non-linear causal relation is not intuitively understandable, and is yet not fully explored. T. Remtema *et al.* pointed out that localized heating of a comb-shape resonator shifts its resonance frequency by 6.5%, compared to the 1% shift in overall heating [49]. H. Sadeghian gave an explanation which was based on the complex coupling of the temperature profile from localized heating with the structure of a microcantilever, especially with the clamping part where the softening effect is the strongest [44]. A more systematic demonstration was published by F. Aguilar Sandoval *et al.* [15]. A pure mathematical analysis was carried out on microcantilevers to reveal that the frequency shift in a certain eigenmode is related to the average value of a weighted temperature profile, while the weight is actually the local curvature function of the cantilever in this same eigenmode. This theory does not only explains the non-linearity brought by non-uniform temperature distribution, but also makes clear why the resonance frequency shift varies from mode to mode, as observed in former experiments [45][15]. However, the SMR is far more complex structurally, and whether these conclusions obtained from solid cantilevers also apply to SMR still remains a question.

1.4.10. Effects of liquid

While the density of a target particle is characterized by the density of its carrier liquid, the role of the liquid as a variable itself participating in the heat transfer process on SMRs is usually ignored, partly because of the difficulty in instantaneous sensing and quantification of the many physical properties of the liquid when it is running through the microchannel, e.g. its temperature, thermal conductivity and density. In fact, heat convection occurs between

the liquid and outer solid structure unless the temperatures of the two are identical, and a different thermal conductivity from the solid results in a distinct conduction process within the liquid which produces an interior temperature profile that cannot be predicted from the temperature profile of the solid part. As the density of the liquid changes with temperature, the actual liquid density would deviate from the reference value which should be measured beforehand, and an error arises. Moreover, thermal conductivity, viscosity and other properties are also temperature-dependent. Therefore, the whole process is in a highly dynamic state, and can only be simulated and investigated in a simplified approximate manner.

1.5. Research Questions

The overall thermoelastic coupling network is shown in Figure 1.19. Solid lines represent directly causal effects, and dashed lines represent coupling effects that are non-causal or yet unidentified.

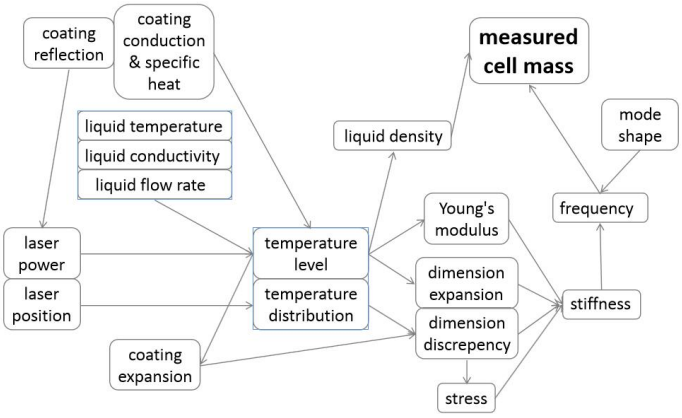

Figure 1.19: Overall thermoelastic coupling network

As the most efficient and compatible method to sense the vibration of an SMR, optical detection also brings about problems that are attracting more and more attention. It heats the device to a considerable temperature level, posing threats to changing the material properties and even damaging the device and biological analytes, which greatly undermines its longevity and reliability. Although several studies concerning thermoelastic effects have been carried out, they basically examined individual factors on cantilevers rather than the comprehensive effect from their interaction. Moreover, the more complex structure of the SMR than the normal cantilever leaves the validity of their conclusions under question. In order to investigate to what extent do these factors affect the result of mass measurements using SMRs, and fill the blank in this field, the main research question is proposed:

How much error is induced by the thermoelastic coupling effect in the mass sensing using suspended microchannel resonators?

The main question can be divided into two subquestions:

- ***How does the coating thickness affect the precision in the mass sensing using suspended microchannel resonators?***
- ***How does the liquid filling the suspended microchannel resonator affect its precision in the mass sensing?***

Concerning these questions, a research plan is made.

1.6. Research Plan

The resonance frequency shift of SMR caused by the thermoelastic effect originates from a series of physical phenomena, including heat transfer, thermal expansion and stiffness variation. Studying these physical laws quantitatively would be the first step to comprehend the whole network.

Before experiments, simulations shall be carried out in the software to obtain a theoretical vision on the phenomena that are expected to happen in the experiments, and to serve as a precaution that provides an opportunity to discover conditions under which fails happen, so that they can be avoided in the experiments.

Several aspects linked to the experiments are raised.

1. *Test the mass sensitivity of the SMR*

   Mass sensitivity is a quantitative value that connects the variations of frequency and mass. In our setup, the frequency of SMR is directly measured, but the mass of the analyte is the wanted information instead. If the mass sensitivity is known, the mass error brought by conditions like sensing laser and coating can be evaluated according to the frequency shift they cause. We will test the mass sensitivity of the SMR with liquids with known density.

2. *Evaluate the effect of temperature distribution of the SMR*

   The temperature distribution is basically determined by the laser position on the SMR. The specific temperature distribution pattern for each selected laser position can be obtained in the simulation. In experiment, the laser will be focused on the same positions as in the simulation. Therefore, the correspondence between temperature distribution patterns and frequency shifts of different eigenmodes can be known.

   It is notable that, since the frequency shift is related to the coupling between temperature distributions and mode shapes, the laser position could also be represented by its relative position in the mode shape of each eigenmode.

3. *Evaluate the effect of coating thickness of the SMR and its coupling effect with temperature distribution*

   Experiments will be done on SMR with different coating thickness in order to exploit the effect of changing coating thickness on the resonance frequency shift of SMR. Afterwards, we will do experiments concerning both the two variables of coating thickness and laser position, to see the coupling effect of these two factors.

4. *Evaluate the effect of coating on the resonance frequency stability of SMR*

   The vibration of both uncoated SMR and coated SMR during a period of time will be monitored. A frequency counter is used to count the peaks within different sections of this period, so the average frequencies over time can be calculated, and their root mean square serve as a parameter for the stability of the SMR.

5. *Test the effectiveness of coatings in improving the detection limit of SMR*

   For SMR samples without coating and with different thickness of coatings, the lowest detectable signals will be measured, and will be converted to the mass detection limits.

In addition, we will build a temperature-controlled chamber if it is achievable in our lab. In such a chamber, SMR will be overall heated, so the temperature is uniform anywhere on it. By doing so, the influence of temperature distribution is removed. The resonance performance of such SMR is compared to the locally heated ones to further interpret the effect of temperature distribution. Also with this chamber, the SMR can be maintained at an optimum temperature level, such as room temperature, so all the thermoelastic coupling effects can be eliminated at once.

1.7. Risks and Countermeasures

1.7.1. Unrecognizable peaks out of excessive noise on the spectra under heating condition

Noise comes from the background environment, the experiment setup, and the sample itself especially when it is being heated. Conventionally, the intensity of the detecting laser beam is increased in order to raise the signal intensity. In cases where the laser intensity is difficult or impossible to change, the focus can be further adjusted to locate more accurately on the surface of the sample. Actions that decrease the noise can also be taken. This includes adopting setups with lower system noise, working in odd hours, and isolating environmental vibrations with a buffering platform.

1.7.2. The real temperature distribution is not really know

The temperature distribution of an SMR under the detection laser is simulated in softwares. However, the actual temperature distribution may differ from the simulation result, which could cause an error. Therefore, the simulation result must be at first validated using cases where the temperature distribution is known.

2

Precision Error in Mass Measurements using Metal-coated Microchannel Resonators

Precision Error in Mass Measurements using Metal-coated Microchannel Resonators

September 23, 2019

The suspended microchannel resonator is one of the most reliable devices for the mass measurement of biological and chemical specimens. Since it works in vacuum, the energy dissipation is decreased to the minimum. In this case, the instability related to the thermoelastic coupling effect has become a major source of uncertainty and a main hindrance for higher mass precision. In order to explore methods to control the thermoelastic coupling effect, we investigated factors that are relevant to the instability in eigenfrequency measurements, including the thickness of metal coating on the top of the resonator, and the position of the detecting laser spot on the resonator. We found that this instability-induced error is 1 to 2 orders of magnitude lower on resonators without coating than on those with coating, and 3 to 4 orders of magnitude lower if the measurement is done with the first flexural eigenmode than with the first torsional mode. The minimum mass error is achieved when measuring the first flexural eigenmode on an uncoated suspended microchannel resonator. It is in the magnitude of zeptogram (10^{-21}g), and can be smaller than the minimum detectable mass change which is limited by the minimum detectable frequency change in the measurement.

1 Introduction

The demand for mass measurement is ubiquitous in various industries, and the requirement for accuracy is becoming more and more crucial in chemistry [5] and biomedicine [8] as these industries are going down to smaller scales. However, conventional methodology and instrumentation usually work for substantial mass, which severely limits the mass resolution. The invention of microresonator presents a solution to this problem. This device can effectively improve the resolution of mass measurement via both its working principle and miniaturized scale.

Unlike traditional mass measurement techniques that focus on the mass-force relation, the microresonator exploits the contribution of the effective mass of a structure on its eigenfrequencies, which can achieve high sensitivities through miniaturization [2]. While excited at selected frequencies and its vibration detected with sensing devices, any change in its effective mass can be easily captured and determined by looking at how much its eigenfrequencies shift. With photolithography, etching and other precision fabrication processes, it has been successfully scaled down to the micrometer level, facilitating measuring extremely small amount of samples with extraordinary high resolution in eigenfrequency change.

The suspended cantilever is the most common shape for microresonators. When working in fluid, it is widely used to measure the mass of cells or molecules that adhere to the functionalized surface of the cantilever. One of the major disadvantages of this aqueous application is the high damping, namely the degradation of quality factor (QF), which directly affects the frequency resolution. The surrounding fluid also increases the effective mass of the vibrating body, introducing a large error in the determination of the real mass of our target specimens.

The QF degradation is overcome by the design of suspended microchannel resonator (SMR) by [3]. Instead of having an external cantilever-fluid interface, a microchannel allowing for fluid flow is incorporated inside the cantilever body, creating an internal cantilever-

fluid interface. Then, the SMR can be placed in vacuum to avoid high viscous damping. With this innovation, the QF can be up to 15000 [4], two orders of magnitude higher than in aqueous environment.

But it leads to a new problem. We sense the SMR's vibration by exploiting the Doppler effect of a detecting laser beam. When there is little medium in the surrounding, the heat brought by the laser will accumulate inside the SMR instead of dissipating via convection, resulting in a time-varying and location-varying temperature profile on the SMR. Through the thermoelastic coupling effect, the effective stiffness of the device becomes unstable in both time and space, and its eigenfrequencies perform poor stability. This phenomenon is more evident on SMRs with metal coating due to the bi-layered structure. Up to date, such eigenfrequency instability has rarely been reported, and its mechanism has not been fully understood because of its complexity.

In this paper, we will study three factors that are relevant to the thermoelastic coupling effect on the SMR - the incidence position of the laser, the coating thickness and the fluid filling - and how much mass error each of them causes by triggering eigenfrequency shift as well as degrading eigenfrequency stability and QF.

2 Sample Details

The sample we use consists of two parts: the chip with a free-vibrating SMR, and an interface with reservoirs as well as inlet and outlet for the fluid.

2.1 SMR chip

The chip is made of silicon dioxide and fabricated by several steps of deposition and etching. The SMR is in the form of a U-shaped tube and is suspended at the front of the chip to allow free, independent vibration of the two legs. The leg ends are attached onto the chip and connected respectively to two holes that are open on the back of the chip (See Figure 1). The dimensions are listed in Table 1.

Table 1: *Dimensions of the sample.*

Parameter	Value (μm)
Chip length	2900
Chip width	2200
SMR length	205.2
SMR height	3.5
SMR width	28
SMR leg width	11.3
Gap between the legs	5.4
Fluid channel height	2.5
Fluid channel width	9

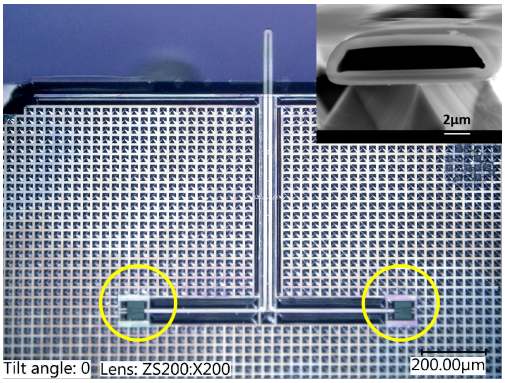

Figure 1: *The sample chip imaged with a digital microscope. The yellow circles highlight the opening to the reservoirs. The symmetrical design allows the two-way flowing of fluid. The inset shows an SEM image of the cross-section of the microchannel.*

2.2 Fluid interface

The interface is 3D printed by a Envisiontec 3D printer using acrylic resin. A schematic of its structure is shown in **missing fig**. It has two reservoirs, which are connected to an inlet and an outlet respectively. The chip is glued on the top of the interface, inside a groove that ensures the alignment between the two parts. The docking between the two holes on the chip and the two reservoirs on the interface completes a path for liquid through the SMR.

3 Continuous Eigenfrequency Measurement

In modal analysis, the common practice is to excite the sample with a signal, collect the velocity information from the Doppler vibrometer and do Fourier transformation to get the frequency-velocity spectrum. However, eigenfrequency stability is also a major parameter to be studied in our work, so we need to enable continuous eigenfrequency measurement against time.

3.1 Setup

One main advantage of the SMR is its high QF because of the absence of viscous fluid around it. Since liquid is sealed inside the SMR, we should also avoid air by creating a vacuum environment where the SMR can be installed. We build a multi-function chamber that can connect to a vacuum pump through a hose on its back sidewall. On the bottom of the chamber is a fixed magnet base on which a clamper used to clamp the SMR sample is installed. A piezoactuator under

the magnet base is responsible for transmitting the excitation to the sample through an interface on the front sidewall of the chamber. There are two needles on the lateral sidewalls of the chamber through which the liquid can be exchanged between the SMR and the environment. Figure 2 shows a picture of the chamber.

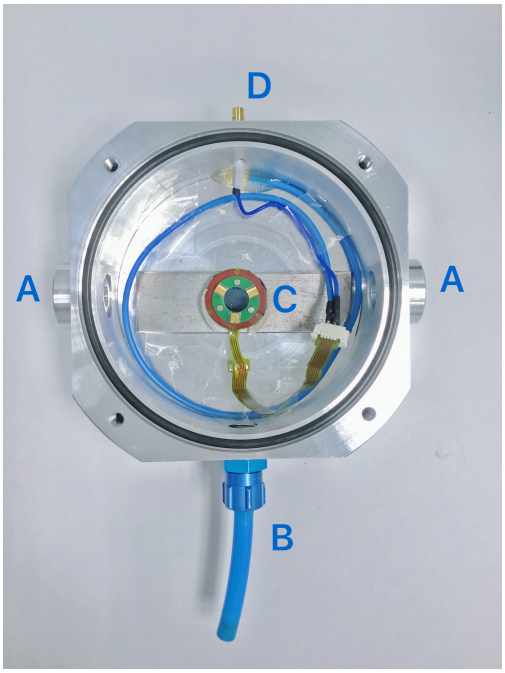

Figure 2: *The multi-function vaccum chamber. A: needles for fluid. B: a hose connecting with a vaccum pump. C: the magnet base and the piezoactuator. D: the interface between an excitation generator and the piezoactuator.*

The chamber is connected to a vacuum pump, a liquid delivery pump and an excitation source via corresponding interfaces. On the vacuum pump side, a needle valve serves to roughly control the vacuum level, and the air pressure can be directly read out on a digital gauge. A Polytec MSA-400-PM2-D laser doppler vibrometer (LDV) above the chamber shoots a laser beam onto the SMR, detects the frequency of the reflective laser and sends the data to a decoder, where the data are processed before ready to be shown on a computer. The laser power was measured to be 200μW. For generating the excitation, controlling the measurement and saving the data, we have two choices.

For single-shot measurement, it is more convenient to use the Polytec junction box to generate a random pseudo signal that covers the full range of frequency, and plot the consequent gain-phase spectrum in the Polytec Scanning Vibrometer (PSV) software after a fast Fourier transform (FFT). FFT is a fast way to do Fourier transform with the factorization of discrete Fourier transform (DFT) matrices. However, the software is able to store only one spectrum data at a time, which means only the last one within a continuous measurement is saved. So we use an Agilent E5061B ENA vector network analyzer (VNA) for continuous measurement and the result of each measurement is saved in a continuous way. Different from the junction box, The VNA generates a sweeping signal over a preset range of frequency, and receives the SMR's instant response to every frequency from the decoder. The response signal is then compared to the excitation signal to plot the transmission/reflection (T/R) spectrum in both gain and phase. We further extend the VNA with an external computer so that we can easily control it with MATLAB codes and directly save the data to the hard drive.

Comparatively speaking, the VNA can measure a certain range of frequency, thus is faster and can achieve finer frequency resolution. It also enables continuous data saving. But the ring-down effect on a high-QF resonator strictly limits its sweeping speed, and the communication between it and a computer also prolongs the interval. As a result, the minimum time between measurements, or gate time (GT), is about 11 seconds.

Table 2 lists the comparison between the junction box and the VNA in some aspects.

Table 2: *Comparison between the Polytec junction box and the VNA.*

	Junction box	**VNA**
Excitation	Pseudo-random	Sweeping
Signal process	FFT	T/R
Frequency span	0-1MHz	Flexible
Control	By PSV software	By MATLAB
Continuous measurement	Possible	Possible
Continuous data save	Not possible	Possible

3.2 Experiment configuration

3.2.1 Chamber pressure threshold

The air surrounding the SMR in the chamber shifts the eigenfrequency of the SMR downwards by increasing its effective mass, as well as drags the QF down by stimulating energy dissipation. But its influence is not linear. Since the chamber is not pressure-controlled, we need to find a pressure range within which the pressure-gradients of eigenfrequency and QF are negligible. By measuring the two parameters of the first 3 eigenmodes on an SMR under different chamber pressure, we found that the QFs are near saturation once the pressure was lower than 0.03mbar, and the eigenfrequencies

were hardly affected when the pressure was lower than 0.1mbar (see Figure 3 and Figure 4). The results are consistent with the fact that the average free mean path of air only rises to the same order of magnitude as the dimension of the SMR when the pressure reaches 0.17mbar. Considering the time cost of pumping the chamber to such high vacuum, we set 0.05mbar as a chamber pressure threshold for all the samples we use. The free mean path of air at this pressure is about 680μm. All the experiments were performed with the chamber pressure around this value, and the results are regarded safe and valid.

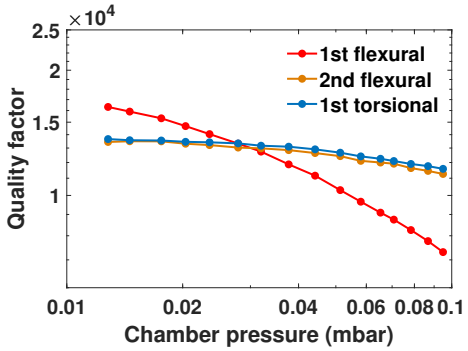

Figure 3: *Quality factors against chamber pressure. The QFs for the second flexural mode and the first torsional mode saturate at around 0.04mbar. The QF for the first flexural mode keeps rising with lower pressure, but is getting less steep. The three curves intersect at around 0.03mbar. Due to equipment limitation, it is extremely difficult to further reduce the pressure when it is under 0.04mbar.*

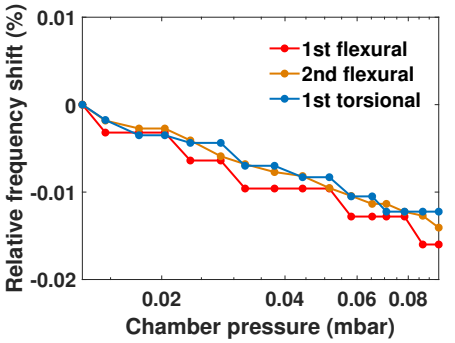

Figure 4: *Eigenfrequencies against chamber pressure. The eigenfrequencies for the three modes decline by less than 0.02% as the pressure rises from 0.01mbar to 0.1mbar, and the decline is barely larger than the resolution (∼1.22Hz).*

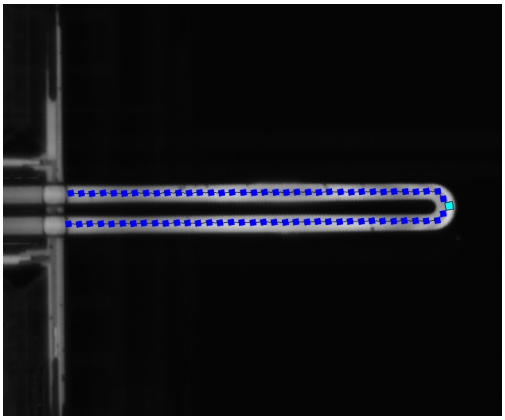

Figure 5: *The grid in scanning measurement.*

Table 3: *Eigenfrequency and quality factor for each mode.*

Mode	Frequency (Hz)	QF
First flexural	146694	13052
Second flexural	861499	4008
First torsional	884940	8222

3.2.2 Sample characterization with single scanning

Under the safe chamber pressure level, the characterization of the SMR sample was carried out using the Polytec junction box. A random pseudo signal in the range of 0 to 1MHz was applied to the sample. With the PSV software, a scanning through a grid containing 73 points along the SMR was done (see Figure 5), and the frequency-velocity spectrum of each point can be checked in the software. The QF of each peak in the spectrum can be obtained by fitting it to a Lorentzian curve. This scanning result provides us with a primary understanding as regard to where the eigenfrequency of each mode falls on the spectrum, and how the quality factor varies with different conditions. Figure 6 shows the spectra of one scanning point near the free end on one sample. The eigenfrequencies and QFs of it are listed in Table 3.

Within 0-1MHz, only three eigenmodes could be covered, including two flexural modes and one torsional mode. The eigenfrequencies of higher modes are unknown, so it is impracticable to find their peaks on the VNA to do continuous measurement since the VNA only sweeps a narrow frequency range. As a result, we only tracked these three eigenmodes in continuous measurement.

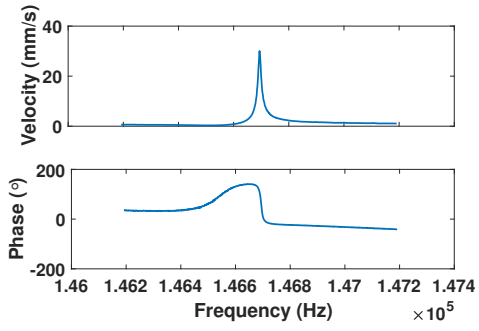

(a)

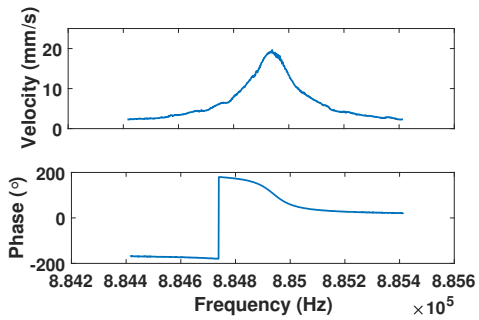

(b)

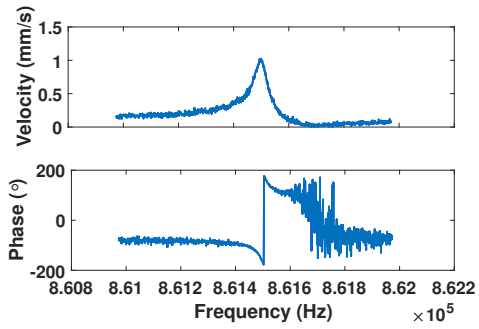

(c)

Figure 6: *Spectra of the first three eigenmodes, measured near the free end on an uncoated SMR with the LDV. (a) The first flexural eigenmode. (b) The second flexural eigenmode. (c) The first torsional eigenmode.*

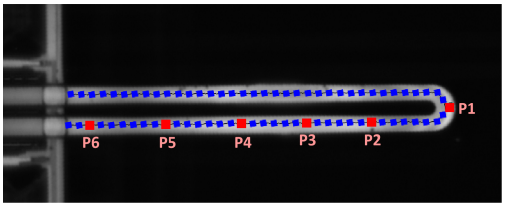

(a)

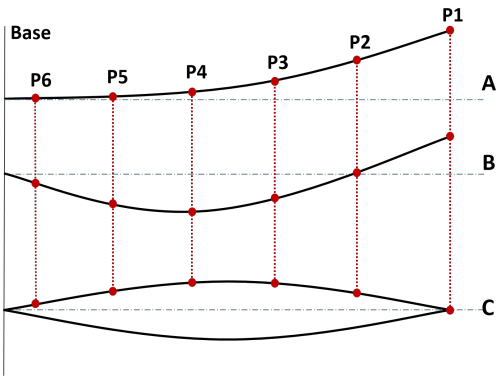

(b)

Figure 7: *The points for continuous measurement (a) in the grid (marked by red squares) and (b) in the mode shapes of the first flexural mode (A), the second flexural mode (B) and the first torsional mode (C) (marked by red circles).*

3.2.3 Variables in continuous sweep

We mainly study the influence of three variables on the error in mass measurement using the SMR: the incidence position of the laser, the coating thickness and the fluid filling.

In order to capture the mode shapes of the three eigenmodes, we picked six laser positions along one leg of the SMR. Figure 7 shows their locations in the mesh and in the mode shapes respectively. It is notable that, the torsional mode measured at point 1 and point 6 can hardly be distinguished in the spectrum because of their weak vibration (see **fig**). Therefore, the torsional mode is not measured at these two points.

The common thickness of coating applied on such SMRs is 6nm. In order to test both thinner and thicker coating, we adapted to the characteristics of our sputter coater (JEOL JFC-1300) and set the coating thickness values to 4nm, 8nm and 12nm. A control group with no coating is also designed. All the coating-related experiments are performed on a single SMR (sample 1), first starting without coating. After each measurement, a 4nm-thick Au/Pd coating was added onto its top surface.

Due to the difficulty to have a sample holding a full

channel of liquid without leaking, we selected two other SMRs (sample 2 and sample 3) for the liquid-filling measurement, one without coating and the other with 8nm coating. All the samples are from the same batch and have the same specifications.

The overview of the variable setting is listed in Table 4. There are 8 scenarios in total.

Table 4: *Variable setting for the experiments.*

Sample	Laser positions	$t_{coating}$ (nm)	Filling
1	6	0	No
		4	No
		8	No
		12	No
2		0	No
		0	Water
3		8	No
		8	Water

3.2.4 Process of data from continuous sweep

In each of the above scenarios, 72 measurements were done non-stop on each of the three eigenmodes, which means we obtained 72 eigenfrequency values for each eigenmode in each scenario. The average value of each set of the 72 data is considered as the steady-state eigenfrequency for the corresponding eigenmode in the corresponding scenario, and the Allan deviation of them is a characterization of frequency stability.

4 Results and Discussion

4.1 Steady eigenfrequency

The eigenfrequencies show a non-linear variation when the detecting laser moves along the SMR. The steady eigenfrequencies measured from 5 locations on the SMR are plotted in Figure 8. The variation may be attributed to the local heating by the laser, which results in a nonuniform temperature profile over the cantilever, as obtained by simulation result shown in Figure 9. When the detecting laser beam is shooting near the free end of the SMR, the heat transferred from the laser to the SMR body is conducted over the whole device, resulting in a higher temperature level on it. While the laser spot moves towards the clamping base, the chip acts as a huge thermal reservoir, taking the heat away more readily, hence less heat will travel through the SMR body. This explanation complies with the performance of the torsional mode, where the steady eigenfrequency increases with the laser spot moving away from the base. Another explanation is given by *et al.* [1] that the coupling between the mode shape and the temperature profile on the SMR determines the eigenfrequency. This is in good accordance with the second flexural mode. The eigenfrequency variation with location reflects its mode shape, and the highest steady eigenfrequency is observed when the laser spot is near the node of the mode shape. However, the eigenfrequency of the first flexural mode shows a non-monotonic and irregular variation. The reason might be the imperfection on the structure of the device, caused by errors during either the fabrication or the coating process. Moreover, it is notable that the eigenfrequencies become more susceptible to the laser position as the coating gets thicker. When there is no coating, the values do not change with the movement of the laser. It indicates a more uneven local stiffness distribution along the SMR when the coating is thicker. The stiffness variation is largely ascribed to the stress between the coating layer and the SMR body that is induced by the differential thermal expansion of the two sides, according to the study by J. Mertens *et al.* [7]. Given the same temperature profile, larger internal stress will arise on thicker coating than thinner coating, which means thicker coating is more sensitive to temperature. Consequently, as the laser spot moves from point to point, the variation of temperature profile will result in a greater variation of stiffness profile, and thus a greater eigenfrequency variation, on SMRs with thicker coating.

We also studied how the eigenfrequencies measured at each location change with the coating thickness (see Figure 10). In general, the eigenfrequencies first drop when a layer of 4nm-thick coating is applied onto a bare SMR, and then rise as the coating thickness increases from 4nm to 12nm. In fact, the coating can affect the eigenfrequency through both mass and stiffness. On one hand, thicker coating adds the effective mass of the vibrating body, reducing its eigenfrequency. On the other hand, greater internal stress from a thicker coating stiffens the structure more, and results in higher eigenfrequencies. Either mass or stiffness could be the dominating aspect under different coating thickness, so the eigenfrequency changes non-linearly with increasing coating thickness.

4.2 Eigenfrequency stability

Generally speaking, SMRs with thicker coating present higher Allan deviation in the eigenfrequencies of all the three eigenmodes, or in other words, poorer eigenfrequency stability, as shown in Figure 11. There are two exceptions whose Allan deviation is extraordinarily high:

1. The second flexural mode on point 2 with no coating.
2. The torsional mode with no coating.

Point 2 is very near to the node in the second flexural mode, so its peak is extremely low, and is largely

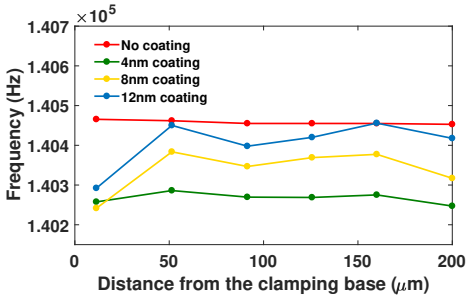

(a) *The first flexural eigenmode.*

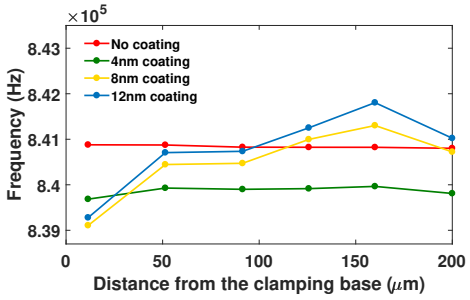

(b) *The second flexural eigenmode.*

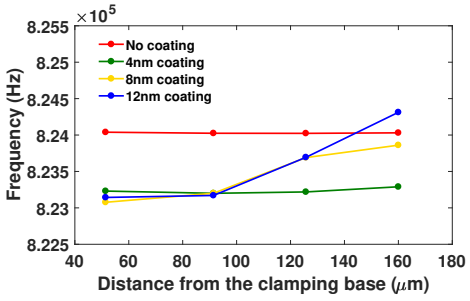

(c) *The first torsional eigenmode.*

Figure 8: *The steady eigenfrequency for each of the three eigenmodes, measured at different locations along one of the SMR legs. Each line represents one coating condition. The errors are too small (1 to 2 orders of magnitude smaller than the frequency variation) so that they could not be displayed in the graphs.*

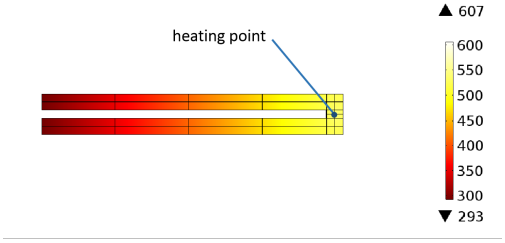

(a)

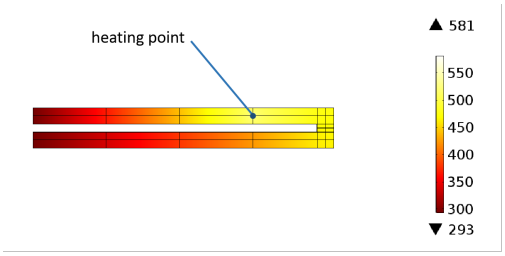

(b)

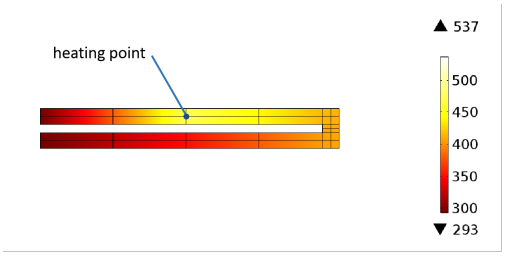

(c)

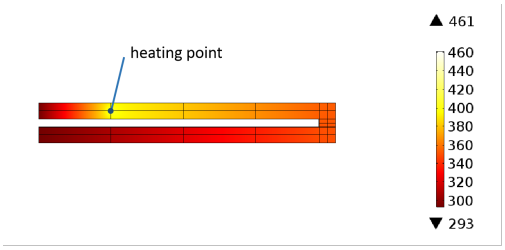

(d)

Figure 9: *The highest temperature appears at the laser spot. As the spot moves towards the base (from (a) to (d)), the highest temperature decreases, and the time needed for reaching an equilibrium also decreases.*

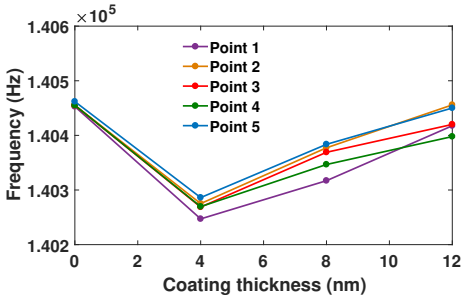

(a) *The first flexural eigenmode.*

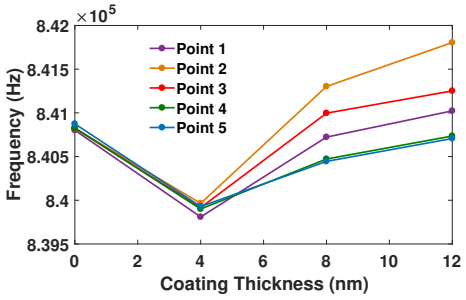

(b) *The second flexural eigenmode.*

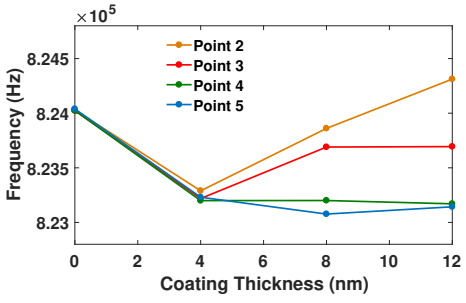

(c) *The first torsional eigenmode.*

Figure 10: *The steady eigenfrequency for each of the three eigenmodes, measured at different coating thickness. Each line represents one point on the SMR. The errors are too small (1 to 2 orders of magnitude smaller than the frequency variation) so that they could not be displayed in the graphs.*

affected by measurement noise. The same is for the torsional mode, which has the lowest peak among the three eigenmodes. This is made even worse when there is no coating on the surface of the SMR, because less amount of the detecting laser is reflected to the sensor, making the signal-to-noise ratio (SNR) relatively low. As the noise adds onto the peaks, it significantly damages the precision of eigenfrequency measurement. Figure 12 shows the spectra of the two cases ((b) and (c)) and their comparison to a normal one (a).

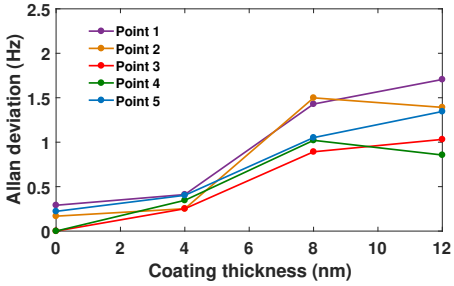

(a) *The first flexural eigenmode.*

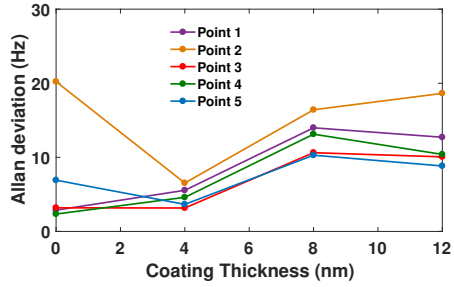

(b) *The second flexural eigenmode.*

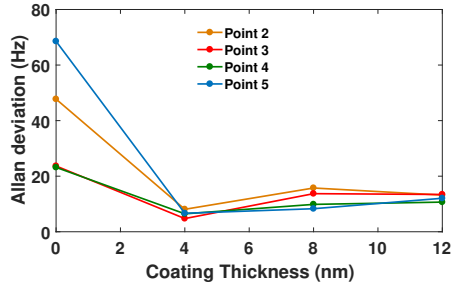

(c) *The first torsional eigenmode.*

Figure 11: *The Allan deviation of eigenfrequency for each of the three eigenmodes, measured at different coating thickness. Each line represents one location on the SMR.*

Typically, to raise the SNR is the main reason for the use of coating on such microresonators. However, it is strongly evident from the graph that the coating is also damaging the dynamic stability of the SMR and

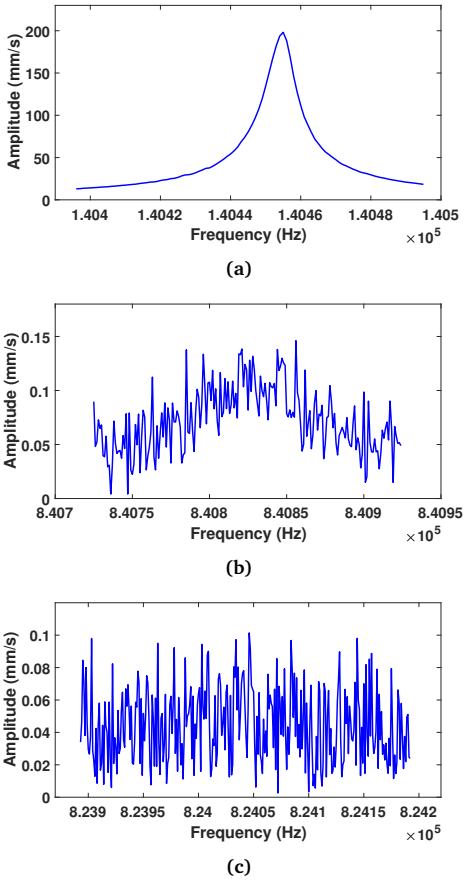

Figure 12: *Rough spectra due to high noise. (a) The first flexural, (b) the second flexural and (c) the first torsional spectra of point 2 on sample 1 with no coating. All data are from the time=0 moment in the continuous measurement on the VNA.*

Table 5: *Thermal conductivity of several substances under room temperature (20°C).*

	Water	SiO_2	Palladium	Gold
Thermal conductivity (W/(m·K))	0.598	1.3	71.8	310

bringing in large precision error. This contradicts to our previous understanding that the coating improves the precision by improving the SNR. Up to date, there is little study on the source of such instability. Meanwhile the additive thermal noise is widely regarded as one of the causes. Considering the high sensitivity of thick coating to temperature variation, it can be inferred that the unstable temperature distribution on the SMR is responsible for its unstable dynamic performance. A further speculation is that the unstable temperature profile is due to the slight drift of the laser spot or the transient heat transfer, but this speculation remains to be verified.

Conclusively, the existence of coating contributes to reduce noise with better signal on one hand, but also brings in the thermal-effect noise on the other hand. Regarding whether to do the coating or not, a trade-off should be made depending on the amplitude of the measured vibration. As the amplitude is low, the coating is beneficial due to the higher signal obtained, as suggested by the first halves of Figure 11b and Figure 11c. As the amplitude is significantly higher than the noise, the precision gets worse with coating, so its thickness should be limited to the minimum, as suggested by Figure 11a and the second halves in Figure 11b and Figure 11c.

4.3 Quality factor

Figure 13 compares how the average quality factor changes with the coating thickness. It can be obviously seen that the sample presents poorer QF and thus poorer frequency precision when it is thicker coated. From the perspective of heat dissipation, it is understandable that the induced stress between the metal coating and the silicon dioxide body generates heat during vibration, dissipating the vibration energy into thermal energy. The thermal energy can be readily conducted away due to the high thermal conductivity of palladium and gold (see Table 5), making it an irreversible dissipation process,commonly referred to as thermoelastic damping [6]. Thus the coating has a reverse effect on the QF.

Interestingly, when filled with water, the QFs got significantly improved, as shown in Figure 14. It is reasonable that the water accounting for a large part of the total mass possesses a great amount of energy during vibration, thus increasing the QF of the system.

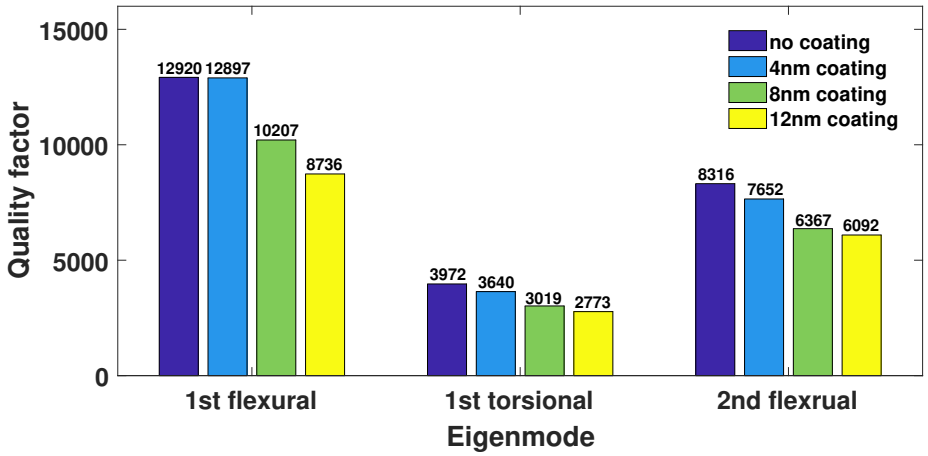

Figure 13: *Quality factor for each eigenmode, comparison among different coating thickness.*

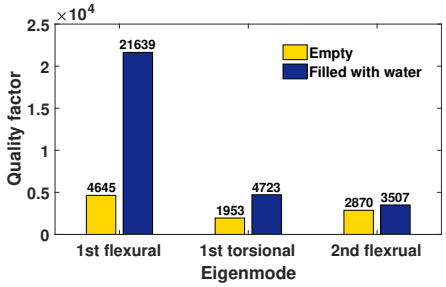

(a) *SMR without coating.*

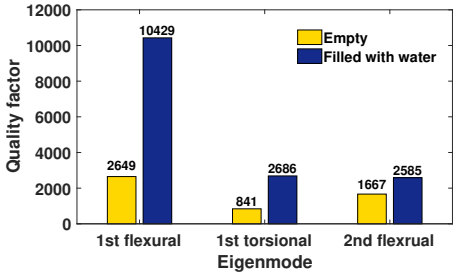

(b) *SMR with 8nm-thick coating.*

Figure 14: *QF for each of the three eigenmodes, measured respectively on (a) one uncoated SMR and (b) one coated SMR, before and after they were filled with water.*

4.4 Mass error

In practical applications, the SMR detects a mass by measuring how much its eigenfrequency shifts when loaded with a mass. This eigenfrequency shift is referred to its original eigenfrequency without the mass load. Although the original eigenfrequency may come out different under different circumstances, it only causes error in its accuracy but not in its precision, and can be minimized by calibration. Therefore, only the Allan deviation, or precision error during the eigenfrequency shift measurement, is what we concern.

The precision errors from our experiments are summarized in Table 6. Note the zero values, which means that the frequency error is below our resolution (1Hz).

In order to translate the frequency error into the mass error, we calculate the frequency-mass responsivity in each scenario.

$$\frac{\partial f_0}{\partial M_{\text{eff}}} = -\frac{f_0}{2M_{\text{eff}}} \tag{1}$$

Here, f_0 is the steady eigenfrequency for each mode in each scenario. The effective mass, M_{eff}, is also related to the steady eigenfrequency:

$$f_0 = \frac{1}{2\pi}\sqrt{\frac{k_{\text{eff}}}{M_{\text{eff}}}} \tag{2}$$

where the effective stiffness, k_{eff}, can be calculated by:

$$k_{\text{eff}} = \frac{4k_B TQ}{f_0 S_x(f_0)} \tag{3}$$

k_B is Boltzmann's constant. T is the ambient temperature during the measurement, and is assumed to

Table 6: *Frequency precision error of each eigenmode at different measuring positions with different coating thickness (unit:Hz). (Flex1: the first flexural mode. Flex2: the second flexural mode. Tor: the torsional mode.) Note that in some cases, the errors measured with the first flexural mode is below the resolution (1Hz), so they do not reflect the actual values*

Coating	Mode	P1	P2	P3	P4	P5	P6
0	Flex1	0.291	0.168	0	0	0.222	0.475
	Flex2	2.872	20.220	3.189	2.347	6.914	7.085
	Tor		47.734	23.663	23.171	68.552	
4nm	Flex1	0.411	0.252	0.252	0.346	0.402	0.222
	Flex2	5.549	6.532	3.160	4.599	3.651	2.907
	Tor		8.081	4.740	6.454	6.643	
8nm	Flex1	1.429	1.499	0.892	1.021	1.051	0.661
	Flex2	13.985	16.418	10.627	13.125	10.289	4.843
	Tor		15.747	13.707	9.850	8.291	
12nm	Flex1	1.705	1.392	1.031	0.856	1.345	0.639
	Flex2	12.712	18.635	10.061	10.395	8.833	3.742
	Tor		13.187	13.418	10.669	12.051	

be 293K since the experiments were carried out at room temperature. $S_x(f_0)$ is the power spectral density (PSD) at the eigenfrequency. PSD reveals how the power of a signal distributes over the frequency. It is measured when a sample is not being excited so that it is only subject to the noise. The power of its response to the noise would mainly concentrate at its eigenfrequencies.

The values of the relevant parameters and the calculation results of the effective stiffness, the effective mass and the frequency-mass responsivity are listed in Table 7.

Finally, combining Table 6 and Table 7, the translated mass precision errors are given in Table 8 and plotted in Figure 15.

Generally speaking, the mass precision error of a coated SMR is 1 to 2 orders larger than an uncoated counterpart. On the same SMR, the mass precision error of measuring with the torsional mode is 3 to 4 orders larger than the flexural modes. When measured on an uncoated SMR using its first flexural eigenmode, the minimum mass error is below the mass resolution of the device (in zeptogram level, e.g. 10^{-21}g), so the result should be sufficiently reliable.

5 Conclusion

In this paper, we investigated the error of mass measurement using an SMR caused by the frequency instability of the device. The experiments were performed in vacuum ($\sim$0.05mbar) with different configurations, including different thicknesses of the metal coating on the SMR, different positions of the sensing laser spot, and the filling of water. The results were analyzed corresponding to each of these variables. It is found that the coating influences the eigenfrequency via both the effective mass and the effective stiffness. Also, it degrades the eigenfrequency stability when its amplitude is significantly higher than the noise, giving it larger variations with changing laser position and in time. When doing measurements on a coated SMR, the mass precision error can be 1 to 2 orders greater than it from measurements on an uncoated SMR. For a single SMR, measuring its torsional mode leads to mass errors that are 3 to 4 orders of magnitude larger than measuring its first flexural modes. The lowest mass precision error appears in the measurements on an uncoated SMR with its first flexural eigenmode, which is lower than the minimum detectable mass change in the measurement, so it has minimum influence on the uncertainty of the result. The quality factor is also severely degraded by thicker coating. However, filling an SMR with water may improve its quality factor significantly. The highest quality factor obtained hereby is more than 21000 from the first flexural mode of an uncoated SMR full of water.

Reference

[1] Felipe Aguilar Sandoval et al. “Resonance frequency shift of strongly heated micro-cantilevers”. In: *Journal of Applied Physics* 117.23 (2015), p. 234503.

[2] Thomas Braun et al. “Micromechanical mass sensors for biomolecular detection in a physiological environment”. In: *Physical Review E* 72.3 (2005), p. 031907.

[3] Thomas P Burg and Scott R Manalis. “Suspended microchannel resonators for biomolecular detection”. In: *Applied Physics Letters* 83.13 (2003), pp. 2698–2700.

[4] Thomas P Burg et al. “Weighing of biomolecules, single cells and single nanoparticles in fluid”. In: *nature* 446.7139 (2007), p. 1066.

Table 7: *Values of parameters to calculate the effective stiffness, effective mass and frequency-mass responsivity, and the calculation results.*

Coating	**Mode**	f_0 **(Hz)**	**QF**	$S_x(f_0)$ **(m^2/Hz)**	$k_{\mathbf{eff}}$ **(N/m)**	$M_{\mathbf{eff}}$ **(g)**	$\lvert\frac{\partial f}{\partial M}\rvert$ **(Hz/g)**
0	Flex1	140473.6	13965	3.05E-15	5.28E-07	6.78E-16	1.04E+20
	Flex2	840949.7	8192	1.06E-18	1.49E-04	5.34E-15	7.87E+19
	Tor	824368.9	4691	3.55E-21	2.60E-02	9.69E-13	4.26E+17
4nm	Flex1	140242.9	12951	9.22E-17	1.62E-05	2.09E-14	3.36E+18
	Flex2	839779.1	7732	2.50E-20	5.95E-03	2.14E-13	1.96E+18
	Tor	823044.4	3566	2.15E-23	3.27E+00	1.22E-10	3.37E+15
8nm	Flex1	140304	9864	3.22E-17	3.54E-05	4.55E-14	1.54E+18
	Flex2	841075.4	6456	4.84E-20	2.57E-03	9.19E-14	4.57E+18
	Tor	823715.8	4035	4.80E-23	1.65E+00	6.16E-11	6.68E+15
12nm	Flex1	140391.8	8945	3.78E-17	2.73E-05	3.51E-14	2.00E+18
	Flex2	841315.9	5483	5.39E-20	1.96E-03	7.01E-14	6.00E+18
	Tor	823938	2753	1.32E-22	4.10E-01	1.53E-11	2.69E+16

Table 8: *Mass precision error of each eigenmode at different measuring positions with different coating thickness (unit:Hz). (Flex1: the first flexural mode. Flex2: the second flexural mode. Tor: the torsional mode.) Note that the frequency errors from the first flexural mode in some cases are below the frequency resolution (1Hz) (refer to Table 6), so the resulting mass errors are below the mass resolution of the device and do not reflect the actual values.*

Coating	**Mode**	**P1**	**P2**	**P3**	P4	P5	P6
0	Flex1	2.795E-24	1.614E-24	0	0	2.135E-24	4.565E-24
	Flex2	3.649E-23	2.569E-22	4.052E-23	2.982E-23	8.786E-23	9.003E-23
	Tor		1.121E-19	5.555E-20	5.439E-20	1.609E-19	
4nm	Flex1	1.224E-22	7.493E-23	7.493E-23	1.030E-22	1.198E-22	6.608E-23
	Flex2	2.831E-21	3.332E-21	1.612E-21	2.347E-21	1.863E-21	1.483E-21
	Tor	2.398E-18	1.406E-18	1.915E-18	1.971E-18	1.863E-21	1.483E-21
8nm	Flex1	9.280E-22	9.733E-22	5.793E-22	6.629E-22	6.828E-22	4.291E-22
	Flex2	3.060E-21	3.593E-21	2.325E-21	2.872E-21	2.251E-21	1.060E-21
	Tor		2.357E-18	2.052E-18	1.474E-18	1.241E-18	
12nm	Flex1	8.527E-22	6.958E-22	5.156E-22	4.279E-22	6.727E-22	3.196E-22
	Flex2	2.119E-21	3.106E-21	1.677E-21	1.732E-21	1.472E-21	6.236E-22
	Tor		4.902E-19	4.988E-19	3.966E-19	4.480E-19	

[5] MF Khan et al. “Online measurement of mass density and viscosity of pL fluid samples with suspended microchannel resonator”. In: *Sensors and Actuators B: Chemical* 185 (2013), pp. 456–461.

[6] Ron Lifshitz and Michael L Roukes. “Thermoelastic damping in micro-and nanomechanical systems”. In: *Physical review B* 61.8 (2000), p. 5600.

[7] Johann Mertens et al. “Effects of temperature and pressure on microcantilever resonance response”. In: *Ultramicroscopy* 97.1-4 (2003), pp. 119–126.

[8] D Sparks et al. “A density/specific gravity meter based on silicon microtube technology”. In: *Proceedings Sensors Expo*. 2002, pp. 171–176.

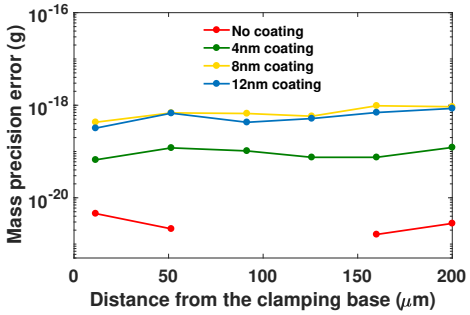

(a) *The first flexural eigenmode.*

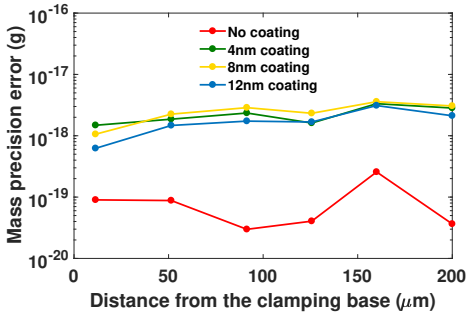

(b) *The second flexural eigenmode.*

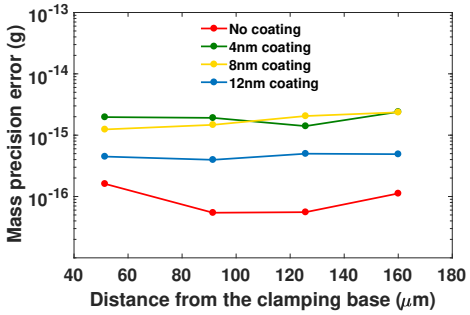

(c) *The first torsional eigenmode.*

Figure 15: *The mass precision error induced by frequency instability, measured at different points on the SMR (unit:g). Each line represents one coating thickness. Note that in subfigure (a), the Allan deviations measured at point 3 and point 4 on the uncoated SMR are 0, so their mass errors equal to 0 and cannot be plotted under the logarithm scale.*

3

Supplementary Material

This chapter includes the origin of the research goal, explains some key decisions in the design of the experiments, and provides supplementary information to the paper.

3.1. Typical Mode Shapes of the SMR

The first three typical mode shapes of an SMR are displayed from Figure 3.1 to Figure 3.3. These modes are mainly studied in this project. A distinction from normal cantilevers is found on its torsional mode, where its two legs are vibrating separately with a phase difference of 180^o.

3.2. Effect of Vacuum Level

When an SMR is vibrating in air, its performance is reduced in two aspects compared to in vacuum. Its vibration amplitude and velocity will decrease due to damping, and its eigenfrequencies will decrease due to additional effective mass. These two aspects can be clearly seen by comparing the respective spectrum of the same SMR vibrating in air and vacuum, as shown in Figure 3.4.

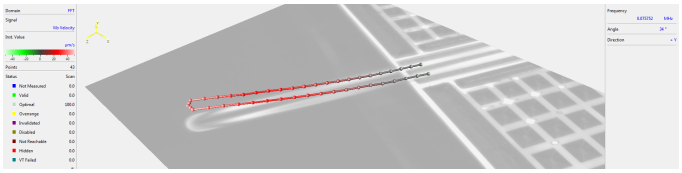

(a)

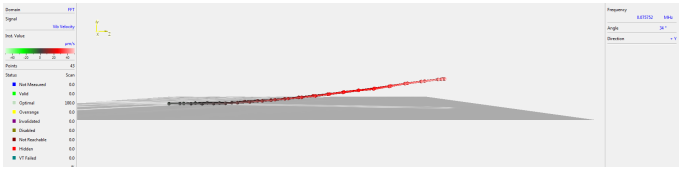

(b)

Figure 3.1: The first flexural eigenmode of an SMR. (a) The overview. (b) The side view.

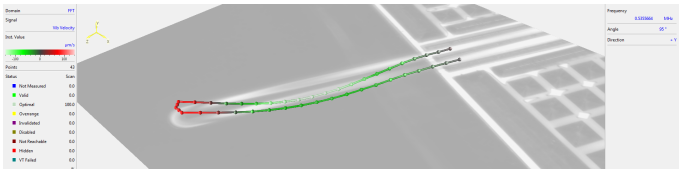

(a)

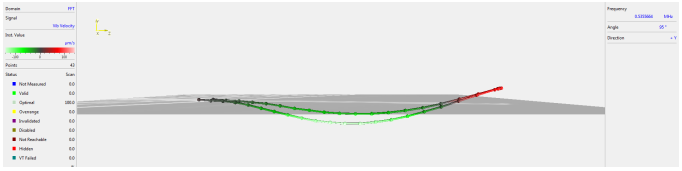

(b)

Figure 3.2: The second flexural eigenmode of an SMR. (a) The overview. (b) The side view.

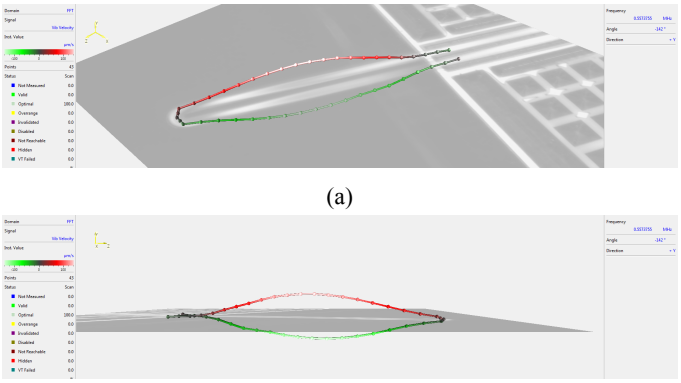

(a)

(b)

Figure 3.3: The first torsional eigenmode of an SMR. (a) The overview. (b) The side view.

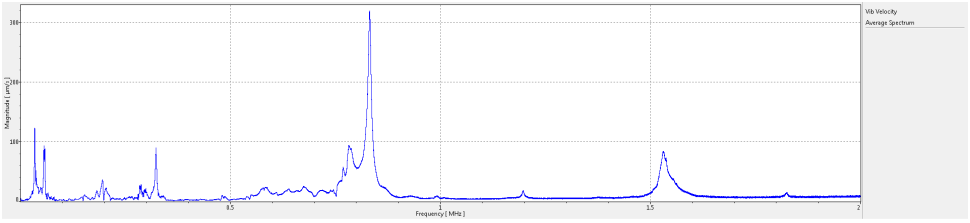

(a)

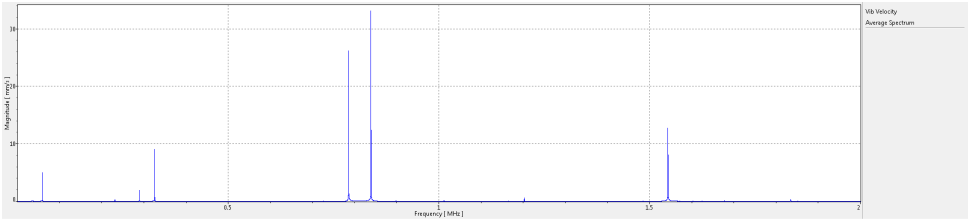

(b)

Figure 3.4: The spectrum of one SMR (a) in air (1184mbar) and (b) in vacuum (0.02mbar). The amplitude in (b) is higher than (a), and the eigenfrequencies are slightly lower.

3.3. Observation of Eigenfrequency Stability

The eigenfrequency stability is rarely reported in literatures, but it was visually observed in our experiment. Figure 3.5 shows the screenshot of a spectrum at different moments. Such spectrum fluctuation is hardly distinguishable on uncoated SMRs, but is quite obvious on coated ones. This greatly damages the precision of measurements on coated SMRs. Figure 3.6 compares the eigenfrequency drift in time of a coated SMR with its uncoated counterpart. The experiment was performed on the LDV with manual control and record. The gate time (GT) is 10s, and the frequency resolution is 1.22Hz.

3.4. Justification of Calculating the Allan Deviation

In previous cases where the stability of a parameter is to be studied, the standard deviation of a collection of data is usually used. However, in Figure 3.6, it is clearly that not only do the eigenfrequencies of the coated SMR fluctuate around their mean values, but the mean values also shift in the upward direction. This is a strong evidence of heat accumulation on the SMR. In this case, the standard deviation contains components from both the transient fluctuation and the long-term shift.

If we want to purely look into the fluctuation, Allan deviation would be a better choice. Unlike the standard deviation that calculates how much the data deviate from their mean value, Allan deviation is about the deviation from one data to the next, so it only concerns the degree of the fluctuation, regardless of the long-term shift.

$$\mathrm{ADEV} = \sqrt{\frac{\sum_{i=1}^{n-1}(x_{i+1} - x_i)^2}{2(n-1)}} \tag{3.1}$$

For the coated SMR mentioned in Figure 3.6, I calculated the standard deviation and Allan deviation of its eigenfrequencies within three time periods: overall (0-600s), first half (0-300s) and second half (300-600s). The results are summarized in Table 3.1, and the comparison between periods can be seen in Figure 3.7. For each eigenmode, there is no significant difference among the Allan deviation of the two halves and the whole period. However, the standard deviation of the first half is about twice as the second half. It is also obviously higher than the Allan deviation in the same period. In the second half, the standard deviation and Allan deviation are roughly equal. It is a strong evidence that there existed both steady shift and fluctuation in the eigenfrequencies in the beginning, and although both contribute to the standard deviation, only the fluctuation is accounted for Allan deviation. After a period of time, the steady shift weakened, so the standard deviation got closer to Allan deviation in value. This validates the effectiveness of Allan deviation in characterizing the fluctuation and leaving out other sources of error.

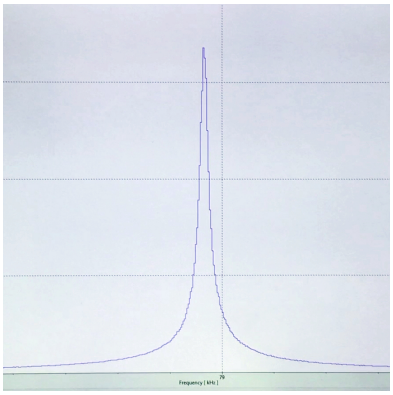

(a) t=7s

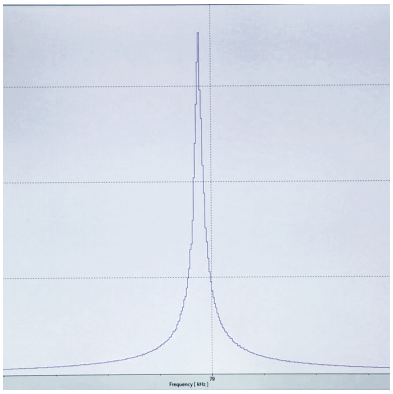

(b) t=19s

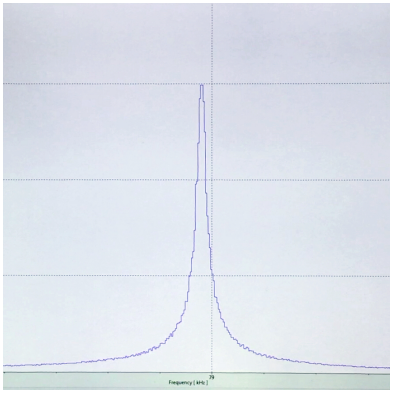

(c) t=34s

Figure 3.5: Spectrum of the 1st flexural eigenmode at different moments in a continuous measurement, measured at the free end of an SMR with 6nm Au/Pd coating.

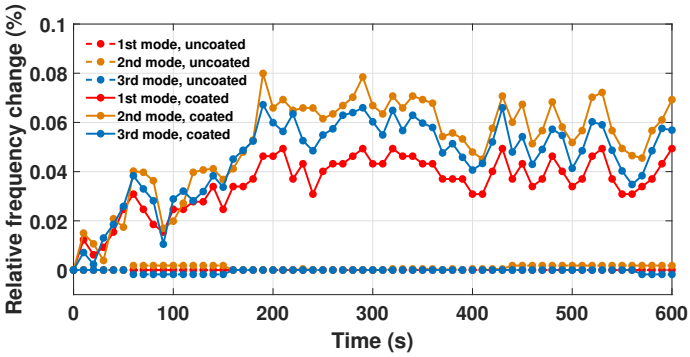

Figure 3.6: Eigenrequency of the first 3 flexrual eigenmodes against time, comparison between two samples with the same specification, one without coating (dashed lines) and the other with 6nm Au/Pd coating (solid lines). The three eigenfrequencies of each sample were measured every 10 seconds simultaneously.

Table 3.1: Standard deviation and Allan deviation of the first 3 flexural eigenfrequencies in 0-600s, 0-300s and 300-600s periods, comparison between two samples with the same specification, one without coating (dashed lines) and the other with 6nm Au/Pd coating (solid lines). The eigenfrequencies were measured continuously (GT = 10s). (Unit: Hz)

	1st flexural	2nd flexural	3rd flexural
Overall SDEV	8.99	95.46	223.20
SDEV, 0-300s	10.45	114.61	270.90
SDEV, 300-600s	5.72	54.32	127.52
Overall ADEV	3.61	33.06	79.58
ADEV, 0-300s	3.76	35.86	78.56
ADEV, 300-600s	3.45	30.01	80.59

3.5. Applying Coating with a Sputter Coater

I used a JEOL JFC-1300 sputter coater to apply Au/Pd coating onto the SMR. Figure 3.8 shows its characteristic curve. With 20mA current, and the deposition rate is around 0.66mm/s. The shortest deposition time allowed on the machine is 5s, which will give a 3.3mm thick coating layer. Since I want to try coating thinner than 6nm, I decided to start with 4nm. This thickness can be achieved by 6s of operation on the machine. However, the recommendation time is 30s. Running it for only 6s may risk imperfection in the coating layer, such as uneven deposition or large error in the thickness.

3.6. Ring-down Effect and Gate Time

When measuring the stability by calculating Allan deviation, the GT should be well controlled. It refers to the time interval after the recording of one data before the next is collected. Only the values of Allan deviation that are computed under the same GT can be used

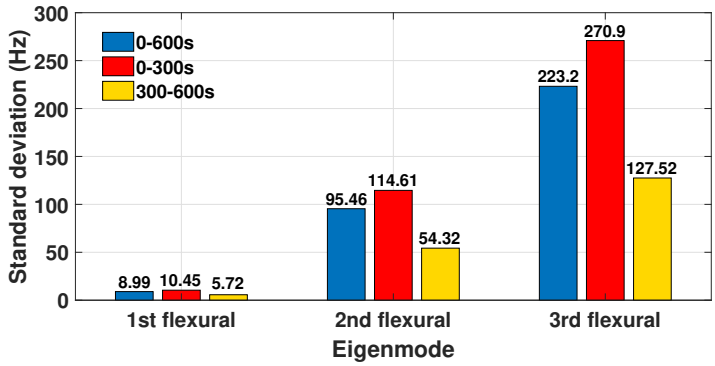

(a)

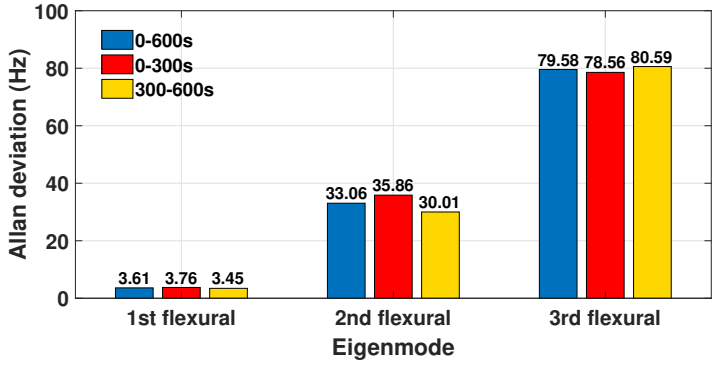

(b)

Figure 3.7: (a) Standard deviation and (b) Allan deviation of the first 3 flexural eigenmodes on an SMR with 6nm Au/Pd coating, comparison between different time periods.

as an index of the degree of stability. It is also practical to record a parameter with different GTs, and its 'Allan deviation-GT' curve reveals the type of noises that are affecting its stability.

I measured the stability of the eigenfrequency by doing continuous modal measurement on the VNA. Typically, VNA works in frequency lock-in mode, namely it only generates signals of a certain frequency. This mode is efficient for a stable eigenfrequency, such as measuring the amplitude of a vibration while the excitation is locked in at its eigenfrequency. Each measurement can finish immediately, so it is very suitable for continuous measurement where transient performance needs to be captured.

However, once the spectrum is fluctuating in time, I cannot speculate the eigenfrequency by only knowing the severity of the sample's vibration at one single frequency. In this case, I made the VNA do continuous sweep over a frequency span that covers the eigenfrequency to be measured. In one sweep, the device gradually increases the frequency of the generated signal. The frequency at which the sample responds the most and vibrates at the highest

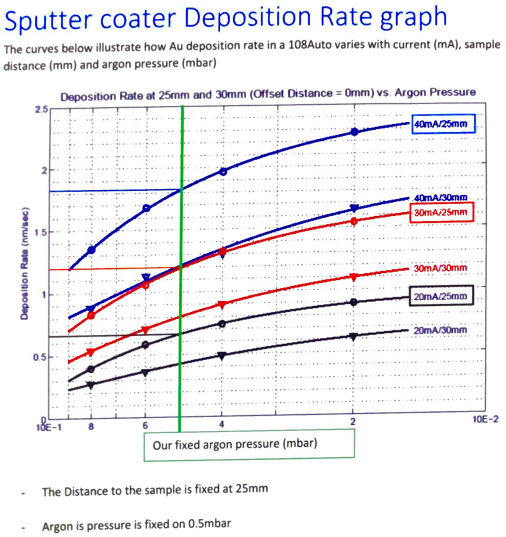

Figure 3.8: Characteristic curves of the sputter coater.

velocity is its eigenfrequency.

The problem is, when the energy is well conserved inside the sample, e.g. it has high QF, its responsive vibration to a lower-frequency excitation cannot be damped out completely before the excitation goes to a higher frequency. The residue vibration will add to the response to the next excitation, and will definitely affect the amplitude. The faster I do the sweep, the more severe the problem gets, as illustrated in Figure 3.9. In order to avoid this so-called 'ring-down effect', I aimed first at keeping the sweep speed low enough, even though this sacrifices the GT. In VNA, the sweep speed is defined by IF bandwidth, a parameter proportional to it.

Besides the sweep speed, the GT is also determined by the number of sweep points in one sweep, or the number of frequency values the excitation adopts in one sweep. Generally, fewer sweep points means fewer workload and thus shorter time, but it also makes coarser frequency resolution if the frequency span is fixed. Considering the strong eigenfrequency fluctuation that could happen, the frequency span should at least be of the magnitude of hundred in order to completely cover the peak while it fluctuates. This asks for a relatively large number of sweep points so as to achieve a relatively fine frequency resolution.

Therefore, trade-off must be made on the IF bandwidth, the frequency span and the frequency resolution, as summarized in Table 3.2.

In order to determine the quantitative relationship between the three parameters, a test was

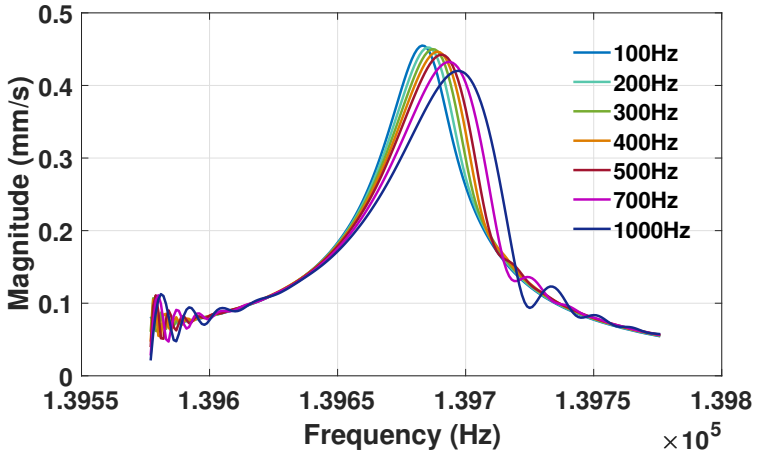

(a)

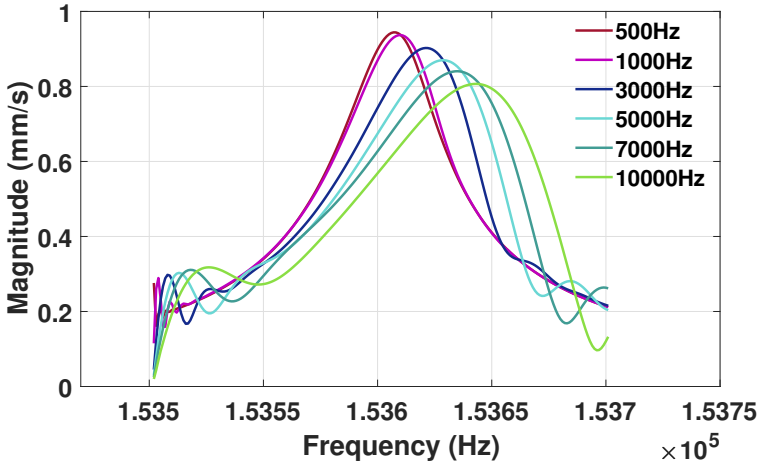

(b)

Figure 3.9: Ring-down effect on two SMRs of the same specifications: (a) without coating and (b) with 8nm Au/Pd coating. Each curve represents one IF bandwidth value. Since the QF of the coated SMR is lower than the uncoated one, it can tolerate faster sweep.

Table 3.2: Summary of restrictions on the selection of parameter values. n_{sweep} stands for the number of sweep points.

	Why should be minimum	**Why should be maximum**
IF Bandwidth	To avoid ring-down effect	IFBW $\propto v_{\text{sweep}} \propto \frac{1}{t_{\text{sweep}}}$
Frequency span	$\frac{f_{\text{span}}}{f_{\text{resolution}}} = n_{\text{sweep}} \propto t_{\text{sweep}}$	To always cover the peak
Frequency resolution	To improve precision	$\frac{f_{\text{span}}}{f_{\text{resolution}}} = n_{\text{sweep}} \propto t_{\text{sweep}}$

carried on the VNA. The results are shown in Table 3.3, and the sweep time can be defined by Equation 3.2.

Table 3.3: Test results of the frequency span, frequency resolution and IF bandwidth on the VNA.

***f* span (Hz)**	**Sweep points**	***f* resolution (Hz)**	**IFBW (Hz)**	**Sweep time (s)**
400	800	0.5	10	76.8
			15	51.2
			20	38.4
			30	25.6
			40	19.2
	400	1	10	38.4
			15	25.6
			20	19.2
			30	12.8
			40	9.6
	200	2	10	19.2
			15	12.8
			20	9.6
			30	6.4
			40	4.8

$$t_{\text{sweep}} = 0.96 \cdot n_{\text{sweep}} \cdot \frac{1}{\text{IFBW}} = 0.96 \cdot \frac{f_{\text{span}}}{f_{\text{resolution}}} \cdot \frac{1}{\text{IFBW}} \tag{3.2}$$

From a pre-experiment, I summarized the frequency span required by a coated and an uncoated sample respectively, as well as the IF bandwidth they can tolerate, as listed in Table 3.4.

Table 3.4: The requirement on the frequency resolution and the IF bandwidth for an SMR without coating and an SMR with a 6nm Au/Pt coating.

	***f* span**	**IFBW**
Uncoated SMR	>100Hz	<20Hz
Coated SMR	>1000Hz	<200Hz

In fact, the selection of the IF bandwidth value on the VNA is limited: 1Hz, 1.5Hz, 2Hz, 3Hz, 4Hz, 5Hz, 7Hz and their ten-fold or power-of-ten-fold values until 300kHZ. For convenience, I selected

$$f_{\text{span}} = 10 \cdot IFBW \tag{3.3}$$

which simplifies Equation 3.2 to

$$t_{\text{sweep}} = \frac{9.6}{f_{\text{resolution}}} \tag{3.4}$$

In order to get a finer resolution and shorter GT than the LDV (1.22Hz and 10s respectively), I finalized that

$$f_{\text{resolution}} = 1Hz \tag{3.5}$$

$$t_{\text{sweep}} = 9.6s \tag{3.6}$$

All our formal experiment conforms to these configurations.

3.7. Experience on Filling SMRs with Water

Filling water into an SMR is our biggest bottleneck throughout this project. Even regardless of the defects from the fabrication, I still have several major difficulties in making the SMRs work well with liquid.

1. No clogging in the channel. The SMR chips are glued onto interfaces by manual operation. The glue has to be smeared onto the interface with a handhold needle, so it is of high risk of getting the glue into the reservoirs and blocking the channel. It also happened that too much glue was applied, so some spread out into the channel when I pressed the chip to the interface to make them stick together. Moreover, two needles need to be glued onto the interface to form a well sealed passage for liquid from the external. So the amount of glue here should be precisely controlled as well, so that it can effectively seal the connection while not clogging the channel.

2. No leakage from the channel. Leakage can happen when the interface, chip and needles are not perfectly fitted, with gaps between them where water can leak out. However, the most common case in our test is a leakage from the SMR body. Because of its extremely thin wall, the SMR cannot stand high fluidic pressure. Initially, I was using a flow-controlled syringe pump to push water into the SMR, so the pressure inside can change drastically and get notably high, especially when the water leaves the reservoir and enters the much thinner SMR channel. Later I changed to an Elveflow microfluidic pump that can do pressure-controlled liquid delivery. But

the pressure needs to be selected carefully - too low pressure is not able to overcome the viscous resistance exerted by the channel wall on water, while too high pressure puts the firmness of the thin channle wall in danger. Actually, the most frequent fail that I experienced on SMRs is the leakage at the corner of the SMR channel due to an excessive pressure.

3. Removal of the water from the SMR channel after filling. After one SMR has been filled and tested, I attempted to empty it for the next use. To do so, I changed among three methods: pumping air into the channel to push the water out from the far end, generating a negative pressure to pull the water out, and heating the sample to speed up the evaporation. Through our attempts, each of the methods proved to be ineffective, or even detrimental to the samples, leading to failures for different reasons.

In order to find qualified samples for our experiment, I tried more than 20 SMRs from five batches. Except those failing due to fabrication errors in their batches or simply our misoperation during gluing, I picked 4 SMRs which have been successfully filled but still reflected some problems. I had a clearer understanding as for why do they fail so easily, under what conditions are they prone to fail and how can I prevent the failing.

All the sample SMRs are named after their batch code (A, B, C,...) and their own serial number within the batches (1, 2, 3,...). The water I used is twice-filtered deionized water.

3.7.1. Sample E1

Sample E1 was first filled with water. It was later dried at 120°C for 20 minutes in order to remove the water. Afterwards, a liquid meniscus was observed inside the channel (see Figure 3.10). This implies residue water in the reservoirs. I then tried adding either positive or negative pressure onto either side of the passage, but it never moved, even under the highest pressure that the pump can put (6bar). I speculate that either the passage is clogged or the viscous resistance between the liquid and the channel walls is too high.

3.7.2. Sample E3

Sample E3 was filled three times within 30 hours, with a pressure of 100mbar to 120mbar, and emptied by negative pressure after each time of filling. It seemed to have been completely emptied for that time being. However, when it was being filled for the fourth time 6 days later, I saw much residue water in it (see Figure 3.11). When trying pushing the water away, I did not see it moving under 150mbar, and had to increase the pressure, which finally resulted in a leakage at 500mbar. It is likely that when I was emptying the sample, the water column became discontinuous because of the height difference between the two openings of one reservoir. Due to the compressibility of air, the water columns at the far side could not feel the applied pressure immediately, so they did not completely exit the channel, leaving residue water in the reservoirs. After being placed in rest for a period of time, the residue water has flown back into the channel, creating such a high viscous resistance that I could not push more water in as easily as before.

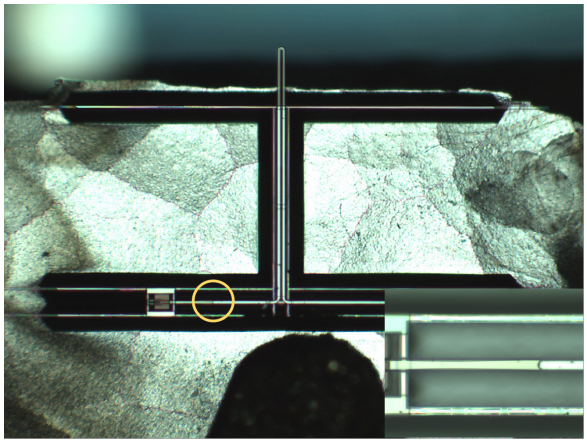

Figure 3.10: A meniscus (marked with the yellow circle) remained inside the channel of sample E1. A zoom-in image is in the inset at the right bottom corner.

3.7.3. Sample F5

Sample F5 was filled very smoothly under 100mbar pressure at first. It was then installed in the vacuum chamber and tested under the LDV, with water still inside it. Accidentally, several bubbles appeared inside the channel after the test. They might be forming under the heating or the vibration. Again, I tried to push the water through to remove the bubbles, but failed to get the water moving. Finally the sample leaked as I increased the applied pressure to 1000mbar.

The sample was then heated to remove the water leaking out, but there was still water inside the channel. Later, I put it again under pressure. Strangely, the leaking began only until the pressure rose to 3000mbar, much higher than it first leaked. Moreover, unlike water that quickly spread out after leaking out of the channel, the liquid leaked rather slowly, and formed an amber-shaped lump (see Figure 3.12a). Neither did it vaporize like water when I heated the sample again, and placed it in rest for a whole night. Instead, it stayed in the same shape, except that a little amount went back into the channel (see Figure 3.12b). It is convincing that the water has got much more viscous, but the reason is unknown.

3.7.4. Sample F6

Sample 6 was not filled with constant pressure. Instead, the water came into several bottlenecks along the channel, so I increased the pressure by a little each time it stopped at one of bottlenecks. The bottlenecks are located at the joints between segments of the channel (see). After the channel was fully filled, the sample was kept under 150mbar pressure for about 1 hour before the water finally came out from the far-side needle (see). I learned from this about how large resistance the water is subjected inside the channel, and how slow it flows therefore.

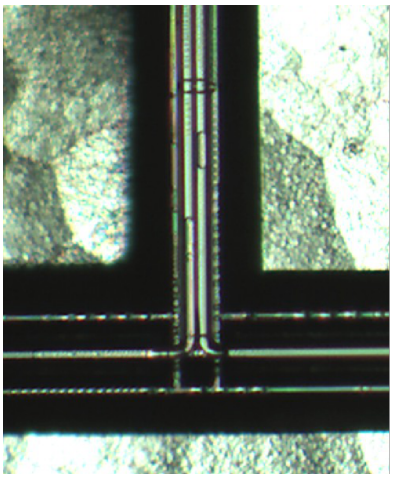

Figure 3.11: Residue water in sample E3 after being placed in rest for 6 days.

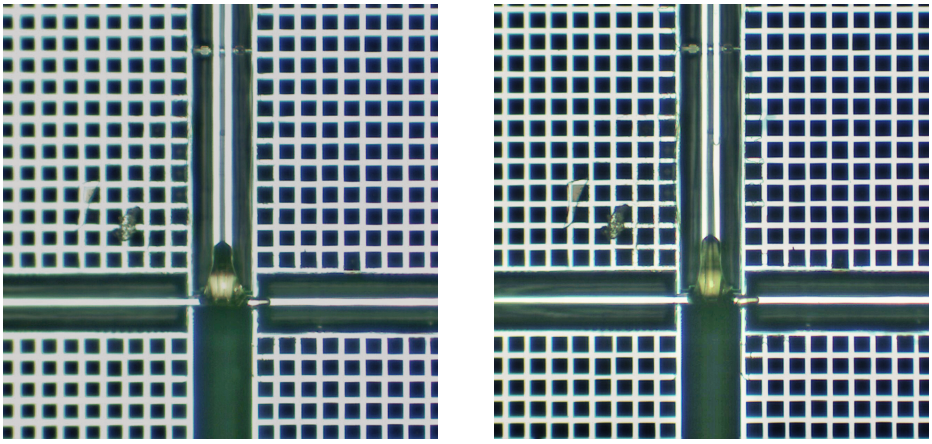

(a) (b)

Figure 3.12: (a) The amber-shaped lump formed by the leaking liquid. (b) The lump did not vaporize, besides, a little amount returned to the channel.

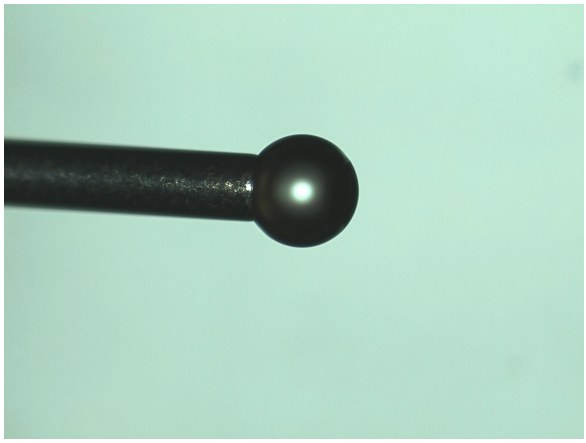

Figure 3.13: The water came out from the needle at the far end from the pump. The SMR was put under 150mbar pressure for about 1 hour.

3.7.5. Tips for the filling experiment

According to what I did on these samples, I hereby give some tips on filling water into such SMRs.

1. If the passage of an SMR is not clogged, the pressure needed to push water into it is 100 to 150mbar. Beyond this range, there is high chance that the sample is clogged.

2. Raising the pressure up to 500mbar will greatly increase the possibility of cracking the channel wall, especially around its corner area.

3. When the water has filled the channel, it starts to flow very slowly. Using higher pressure may accelerate the flow, but it should not exceed the 500mbar threshold in case of causing leakage.

4. Among the three methods to empty an SMR, pushing is extremely slow, pulling cannot completely remove the water from the reservoirs, and heating makes little difference in terms of the evaporation speed of water. Until now, I still have no effective way to get a clean and clear SMR after it has been filled.

5. Every time an SMR full of water is heated, the water becomes thicker and more viscous. The origin of this phenomenon is yet to be investigated, but our speculation is that either the glue or the acrylic resin interface melts and dissolves into the water under high temperature.

3.8. Nonlinearity in the Resonance Spectrum

Nonlinearity exists in every dynamic system in real life. A typical characteristic of nonlinear system is the bending of its resonance peak during forced vibration when its amplitude is too high. In our experiment, the nonlinearity is an important issue I concerned, because I wanted the SMR to vibrate in its linear domain. I achieved this by adjusting the excitation power to a moderate level. However, the nonlinearity is not rigidly relevant to the excitation power, but also affected by the connections from the actuator to the SMR, such as its placement on the clamper and the installation of the clamper on the base. The optimal power for one SMR may not be suitable for another, or even for itself the next time it is used. Therefore, each time before starting the experiments, I tested the nonlinearity of the samples I would be using. Figure 3.14 shows the resonance spectra of one SMR under different excitation power. Usually I selected the highest possible power in the linear domain in order to obtain strong signals.

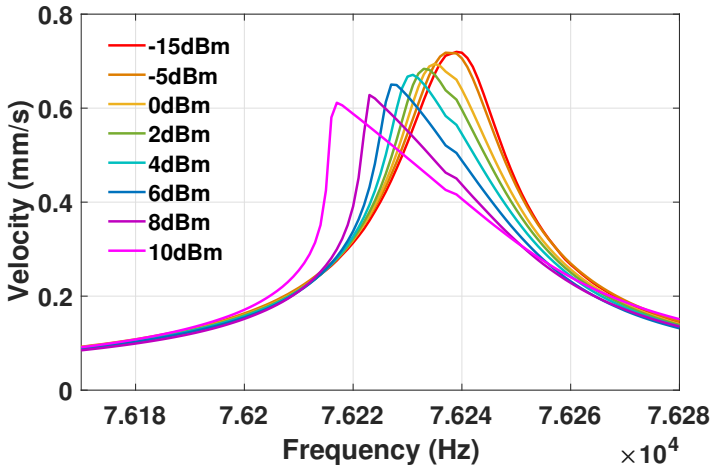

Figure 3.14: Nonlinearity observed on one SMR sample.

3.9. Influence of Laser Focusing

The focusing of the detecting laser is crucial to the precision of our measurement. If the laser is not well focused at the surface of the sample I test, not only will the intensity of the sensed signal get weaker, but the spot may also be dispersed over a large area, so the sensor will be sensing the vibration of a group of points rather than a single dot. In cases where the eigenfrequency depends strongly on the laser position, this could produce large errors. Figure 3.15 displays how the magnitude and phase plots of the first flexural mode changed while the laser spot gradually moved out of focus. An interesting pattern I discovered here is, as the spot was becoming more and more blurred, the eigenfrequency first came up for a

little bit before it went down significantly.

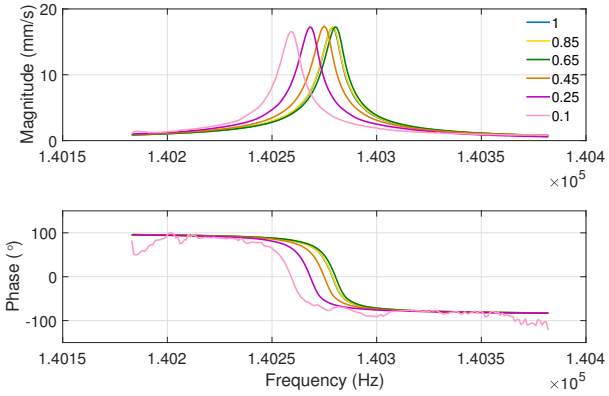

(a)

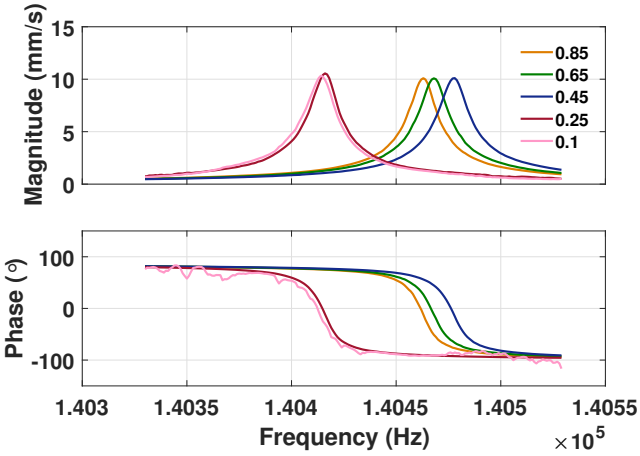

(b)

Figure 3.15: The resonance spectrum of the first flexural eigenmode, measured on the same SMR when it is coated with (a) 4nm thick Au/Pd coating and (b) 12nm thick Au/Pd coating. Each color represents one focusing situation of the laser. The legend shows the normalized laser intensity in the corresponding situation.

3.10. Spectrum Plots against Time

Figure 3.16 to Figure 3.23 plot the 1st-flexural spectra at point 1 at different moments. Each figure represents one scenario. All the measurements were done on the VNA.

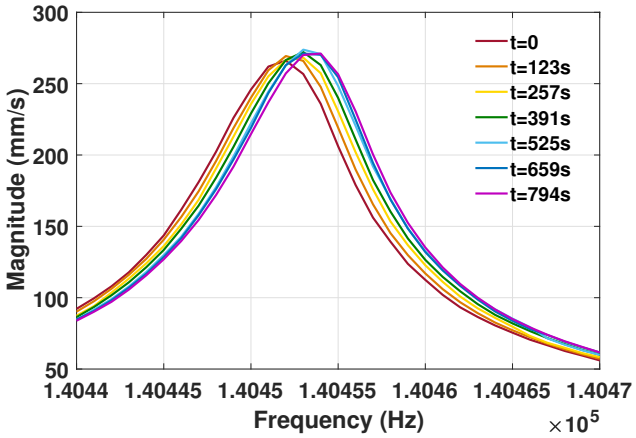

Figure 3.16: 1st-flexural spectra of point 1 at different moments, measured on sample 1 with no coating.

3.11. Spectrum Plots against Laser Position

Figure 3.24 to Figure 3.27 plot the first 1st-flexural spectra (time=0) in the continuous measurements at different locations on sample 1. Each figure represents one coating thickness. All the measurements were done on the VNA.

3.12. Steady Eigenfrequency of Empty and Filled SMRs

The steady eigenfrequency of each eigenmode of sample 2 and sample 3 before and after filling is shown in Figure 3.28.

The eigenfrequency shifts are listed in Table 3.5.

Table 3.5: The relative frequency shift of sample 2 and sample 3 after being filled with water.

	Sample 2	**Sample 3**
1st flexural	12.170%	19.200%
1st torsional	13.663%	18.566%
2nd flexural	12.238%	18.498%

3.13. Allan Deviation against Gate Time

For a set of discrete data, besides the basic GT which is the time interval between two adjacent data, I can also take multiples of the basic GT as new GTs to calculate their corresponding Allan deviation, as shown in Figure 3.29 [50].

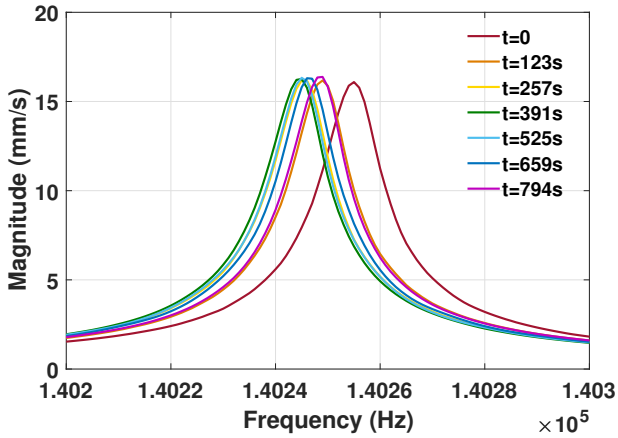

Figure 3.17: 1st-flexural spectra of point 1 at different moments, measured on sample 1 with 4μm coating.

If I take many different GTs and calculate all the Allan deviations, I will be able to plot the Allan deviation curve against its GT. In resonator noise analysis, the slope of the curve reveals information about the type of the noise that the resonator is subject to, as illustrated by Figure 3.30 [51].

To do such noise analysis, the Allan deviation of each eigenmode measured at each point on sample 1 are calculated using different GTs. Because the error of frequency due to its instability is even smaller than the minimum detectable frequency change when the sample is uncoated, it is believed that the noise hereby is negligible. Therefore, only the Allan deviations with the different thickness coating are considered.

Owing to the limited number of data, the curves are too short and not smooth. I only picked some typical ones (see Figure 3.31), trying to figure out the type of the noise.

Basically, no matter how thick the coating is, the Allan deviation curves present an either flat or ascending trend. This corresponds to the segment between bias instability and rate random walk on the characteristic curve.

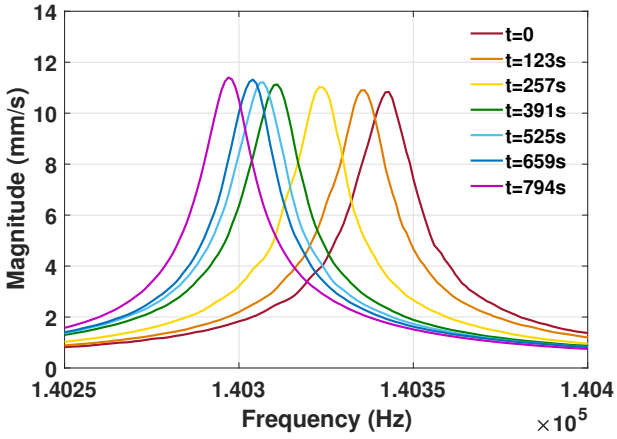

Figure 3.18: 1st-flexural spectra of point 1 at different moments, measured on sample 1 with 8μm coating.

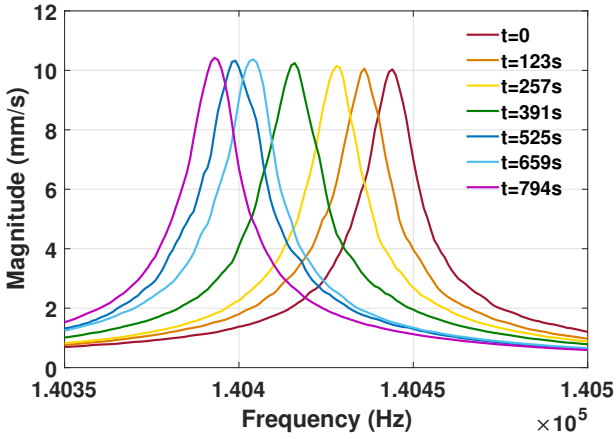

Figure 3.19: 1st-flexural spectra of point 1 at different moments, measured on sample 1 with 12μm coating.

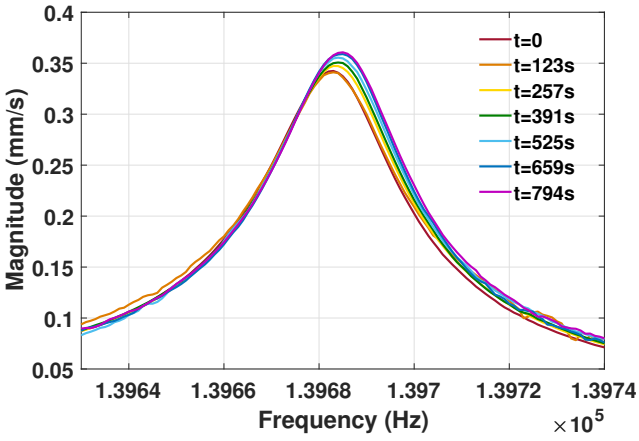

Figure 3.20: 1st-flexural spectra of point 1 at different moments, measured on sample 2 without water filling.

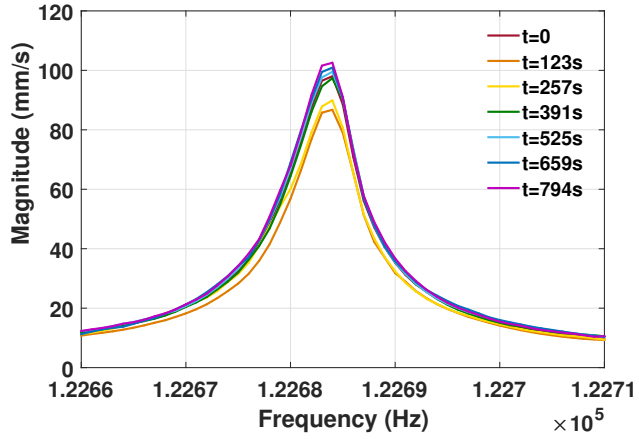

Figure 3.21: 1st-flexural spectra of point 1 at different moments, measured on sample 2 with water filling.

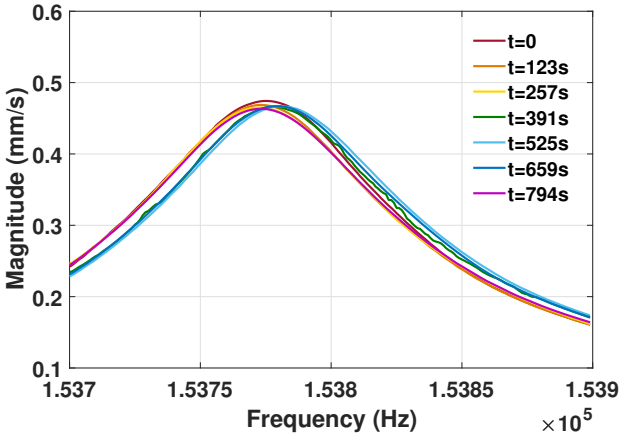

Figure 3.22: 1st-flexural spectra of point 1 at different moments, measured on sample 3 without water filling.

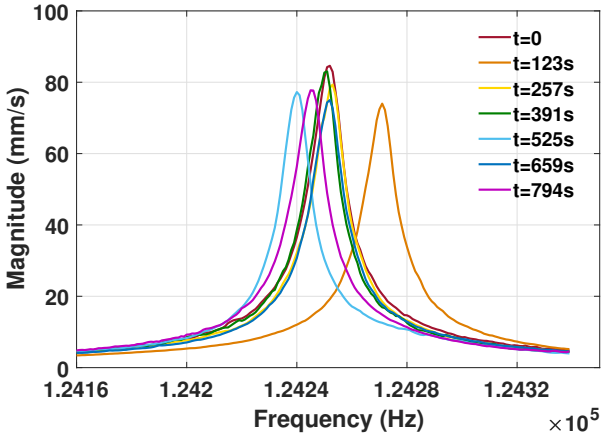

Figure 3.23: 1st-flexural spectra of point 1 at different moments, measured on sample 3 with water filling.

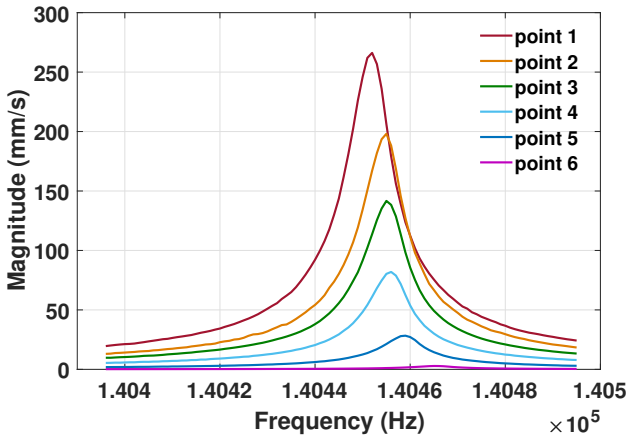

Figure 3.24: 1st-flexural spectra of different locations on sample 1 with no coating, at time=0 moment in the continuous measurement.

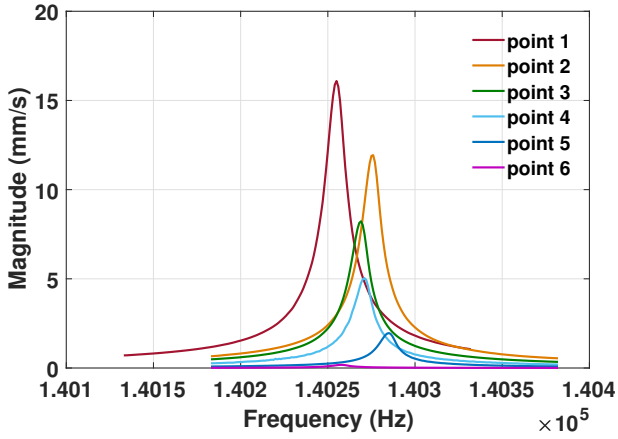

Figure 3.25: 1st-flexural spectra of different locations on sample 1 with 4μm coating, at time=0 moment in the continuous measurement.

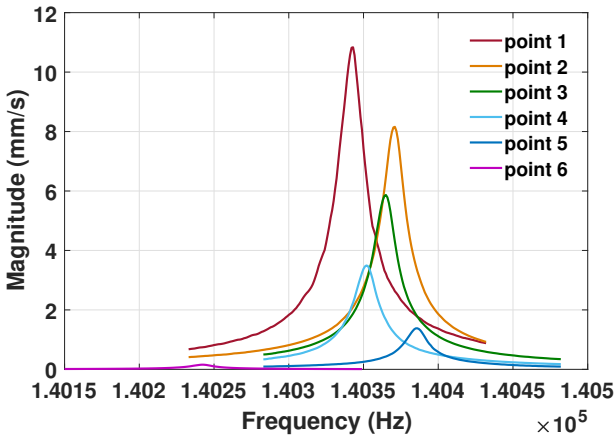

Figure 3.26: 1st-flexural spectra of different locations on sample 1 with 8μm coating, at time=0 moment in the continuous measurement.

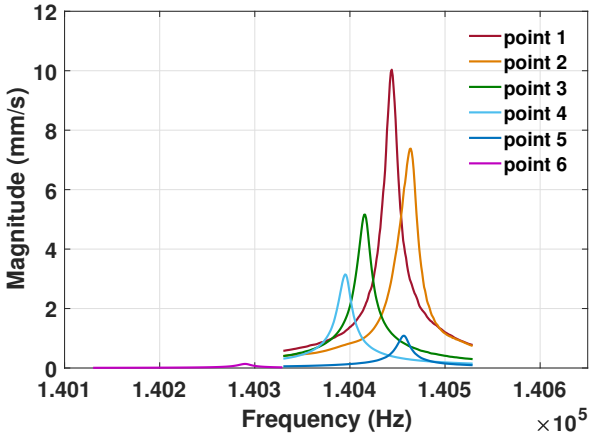

Figure 3.27: 1st-flexural spectra of different locations on sample 1 with 12μm coating, at time=0 moment in the continuous measurement.

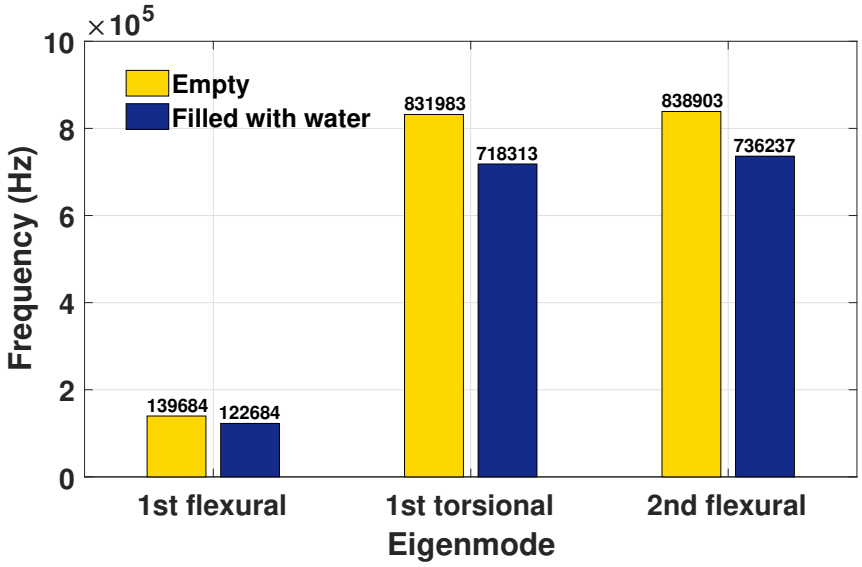

(a)

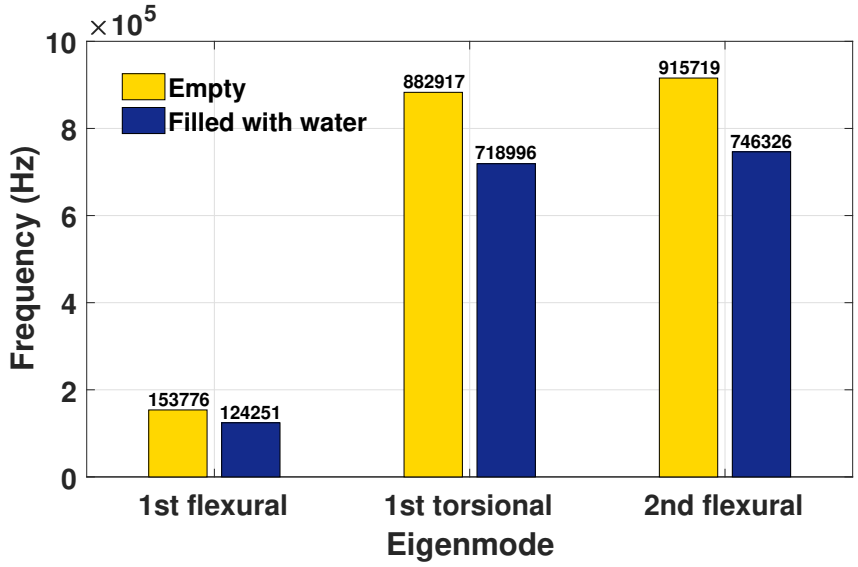

(b)

Figure 3.28: The eigenfrequencies of the 1st flexural, 1st torsional and 2nd flexural modes on (a) sample 2 and (b) sample 3, comparison between the empty and filled conditions.

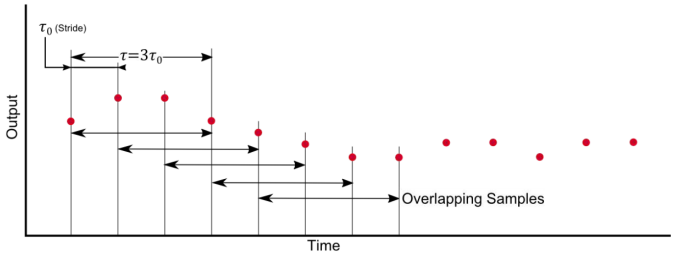

Figure 3.29: The multiple of the basic GT τ_0 can be taken as the new GT τ.

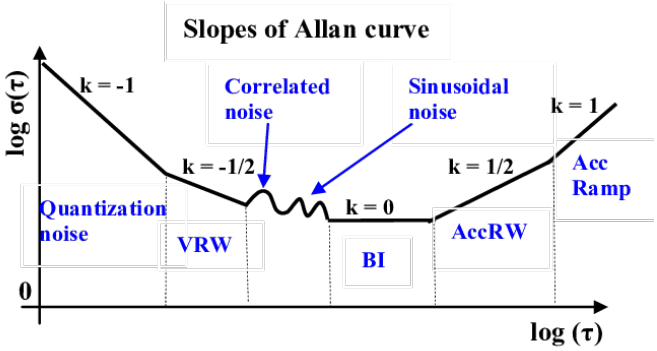

Figure 3.30: The Allan variance characteristic curve against the GT. Allan variance is the square of Allan deviation. VRW: velocity/angle random walk, BI: bias instability, AccRW: acceleration/rate random walk, AccRamp: acceleration/rate ramp.

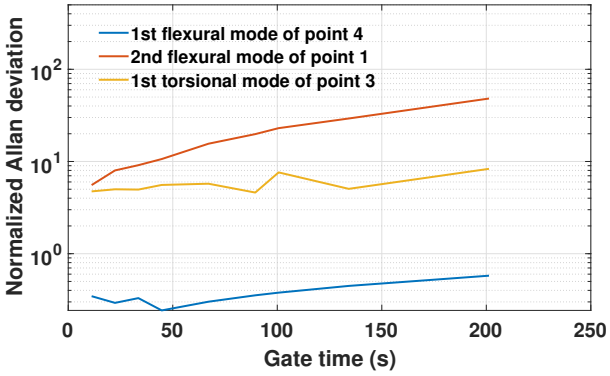

(a)

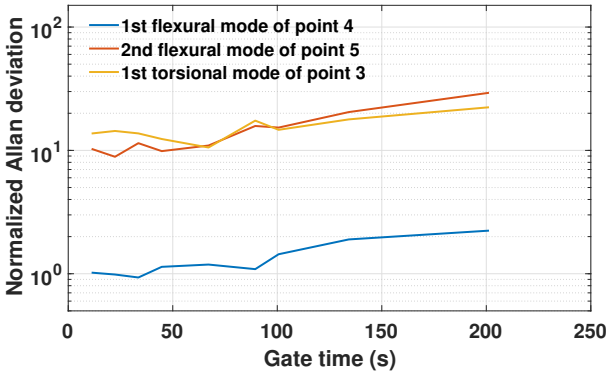

(b)

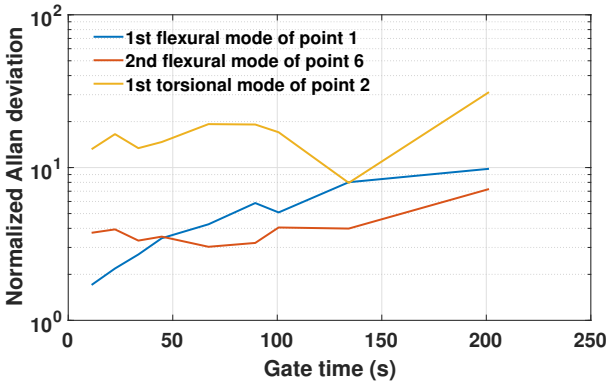

(c)

Figure 3.31: Some typical Allan deviation curves from different eigenmodes on different positions, with (a) 4nm coating, (b) 8nm coating and (c) 12nm coating. For each curve, the Allan deviations are normalized with regard to the value of the shortest gate time (the starting point of each curve).

4

Reflection

In this chapter, a brief reflection upon the project work is given. The timeline of the whole project is summarized and compared to the original plan. During the project, we have met with several major setbacks which forced us to adjust our plan. It is meaningful to look back at our experience in tackling these setbacks. Then, a reflection on my individual development benefit is given .

4.1. Work Timeline

The timeline is listed in Table 4.1.

Table 4.1: Work time line review.

Task	Start date	End date
Literature review	05.09.18	11.03.19
Experiment: characterization of SMRs in vaccum	22.03.19	30.04.19
Experiment: comparison between uncoated and coated SMRs	01.05.19	14.05.19
Feedback: observation of spectrum instability, design of corresponding experiments	15.05.19	11.06.19
Experiment: frequency stability against coating thickness	12.06.19	20.08.19
Experiment: filling SMRs with water, measuring frequency stability	15.07.19	29.08.19

Compared to the original plan, there are three major changes.

1. Redesign experiments regarding the frequency instability. When comparing between the uncoated SMR and the coated SMR, we noticed the poor stability of the spectrum of the coated one. This made our measurements rather imprecise. So we turned our focus to studying how much this instability affects our results, and redesigned our experiment scheme.

2. Adoption of new equipment. In our original plan, all the experiments would be done with the set of MSA equipment. However, in order to finish our newly designed continuous measurements, we adopted the VNA, and spent around two weeks in writing MATLAB codes and characterizing it.

3. Attempts on filling the SMRs with water. At the early stage of our experiment, we have started trying to fill the SMRs. Unfortunately, because of the inadequate quality of the samples, we did not ever succeed for a single time during over three months, and had to wait for new batches again and again. This greatly dragged our progress. Finally, we tried new equipment and new methods and barely got a couple of qualified samples (see section 3.5 for detail), but still had to do our experiments on three samples separately.

4.2. Personal Development

Through this thesis, the most direct benefit for me is the abundant experience in working with high precision devices in a cleanroom. With the strict guidelines that must be obeyed in such a delicate environment, I have become more self-disciplined as well as skillful, making me able to decently handle the jobs. It broadens the possibility for my future development in relevant domains.

I also gained the ability to think in a scientific way. I used to prefer trying before thinking. This might be good for an adventurer, but science is more about wisdom than courage. Being a topic concerning extremely miniaturized size and extremely high precision, the thesis requires a good reasoning before I take every action, otherwise a small mistake could cause a huge loss. I must be conscious of what I will be doing and what precautions I should bear in mind, and must make decisions based on logic instead of arbitrary feeling or intuition. I think this is a necessity for a scientific researcher.

Another enlightenment to me is the importance of interpersonal communication and feedback. In my weekly meeting with my supervisors, I got a lot of helpful suggestions and inspirations from them, which guided me into the correct direction when I got lost. Therefore, I get more and more active in putting forward my own ideas in our discussion, and become more skilled in expressing what I think in a clear and effectively way.

Finally, I am impressed by how tough it is behind the progress of science and technology. The study on the SMR is for the development of a new type of medical test means, which can eventually help to save thousands or even millions of people's lives. My thesis is only

a tiny link within it, and may not make any contribution to the whole progress, but yet it is not as easy as it looks like. There are always aspects that we fail to consider, so we often come into various kinds of trivial accidents, all waiting for us to solve. Only with strong motivation can we persevere and finally find a way through the difficulties. And it is the perseverance of innumerable scholars and researchers together that pushes our world forward. It is amazing.

Bibliography

[1] E. B. Cooper, S. R. Manalis, H. Fang, H. Dai, K. Matsumoto, S. C. Minne, T. Hunt, and C. F. Quate, "Terabit-per-square-inch data storage with the atomic force microscope," *Applied Physics Letters*, vol. 75, no. 22, pp. 3566–3568, 1999.

[2] J. Fritz, E. B. Cooper, S. Gaudet, P. K. Sorger, and S. R. Manalis, "Electronic detection of DNA by its intrinsic molecular charge," *Proceedings of the National Academy of Sciences*, vol. 99, no. 22, pp. 14 142–14 146, 2002. [Online]. Available: http://www.pnas.org/cgi/doi/10.1073/pnas.232276699

[3] M. Shusteff, T. Burg, and S. Manalis, "Measuring boltzmann's constant with a low-cost atomic force microscope: An undergraduate experiment," *American journal of physics*, vol. 74, no. 10, pp. 873–879, 2006.

[4] J. Chaste, A. Eichler, J. Moser, G. Ceballos, R. Rurali, and A. Bachtold, "A nanomechanical mass sensor with yoctogram resolution," *Nature Nanotechnology*, vol. 7, no. 5, pp. 301–304, 2012.

[5] T. P. Burg, M. Godin, S. M. Knudsen, W. Shen, G. Carlson, J. S. Foster, K. Babcock, and S. R. Manalis, "Weighing of biomolecules, single cells and single nanoparticles in fluid," *Nature*, vol. 446, no. 7139, pp. 1066–1069, 2007.

[6] S. M. Knudsen, N. Cermak, F. F. Delgado, B. Setlow, P. Setlow, and S. R. Manalis, "Water and small-molecule permeation of dormant Bacillus subtilis spores," *Journal of Bacteriology*, vol. 198, no. 1, pp. 168–177, 2016.

[7] A. K. Bryan, V. C. Hecht, W. Shen, K. Payer, W. H. Grover, and S. R. Manalis, "Measuring single cell mass, volume, and density with dual suspended microchannel resonators," *Lab on a Chip*, vol. 14, no. 3, pp. 569–576, 2014.

[8] M. F. Khan, S. Schmid, P. E. Larsen, Z. J. Davis, W. Yan, E. H. Stenby, and A. Boisen, "Online measurement of mass density and viscosity of pL fluid samples with suspended microchannel resonator," *Sensors and Actuators, B: Chemical*, vol. 185, pp. 456–461, 2013. [Online]. Available: http://dx.doi.org/10.1016/j.snb.2013.04.095

[9] S. Byun, V. C. Hecht, and S. R. Manalis, "Characterizing Cellular Biophysical Responses to Stress by Relating Density, Deformability, and Size," *Biophysical Journal*, vol. 109, no. 8, pp. 1565–1573, 2015. [Online]. Available: http://dx.doi.org/10.1016/j.bpj.2015.08.038

[10] P. Dextras, T. P. Burg, and S. R. Manalis, "Integrated measurement of the mass and surface charge of discrete microparticles using a suspended microchannel resonator," *Analytical Chemistry*, vol. 81, no. 11, pp. 4517–4523, 2009.

[11] S. Son, M. M. Stevens, H. X. Chao, C. Thoreen, A. M. Hosios, L. D. Schweitzer, Y. Weng, K. Wood, D. Sabatini, M. G. Vander Heiden, and S. Manalis, "Cooperative nutrient accumulation sustains growth of mammalian cells," *Scientific Reports*, vol. 5, pp. 1–8, 2015. [Online]. Available: http://dx.doi.org/10.1038/srep17401

[12] R. B. Karabalin, L. G. Villanueva, M. H. Matheny, J. E. Sader, and M. L. Roukes, "Stress-induced variations in the stiffness of micro- and nanocantilever beams," *Physical Review Letters*, vol. 108, no. 23, pp. 1–5, 2012.

[13] R. Sandberg, W. Svendsen, K. Mølhave, and A. Boisen, "Temperature and pressure dependence of resonance in multi-layer microcantilevers," *Journal of Micromechanics and Microengineering*, vol. 15, no. 8, pp. 1454–1458, 2005.

[14] J. Mertens, E. Finot, T. Thundat, A. Fabre, M. H. Nadal, V. Eyraud, and E. Bourillot, "Effects of temperature and pressure on microcantilever resonance response," *Ultramicroscopy*, vol. 97, no. 1-4, pp. 119–126, 2003.

[15] F. Aguilar Sandoval, M. Geitner, É. Bertin, and L. Bellon, "Resonance frequency shift of strongly heated micro-cantilevers," *Journal of Applied Physics*, vol. 117, no. 23, 2015.

[16] B. A. Bircher, H. P. Lang, L. Duempelmann, C. Gerber, and T. Braun, "Photothermal excitation of microcantilevers in liquid: effect of the excitation laser position on temperature and vibrational amplitude," *Micro & Nano Letters*, vol. 8, no. 11, pp. 770–774, 2013. [Online]. Available: http://digital-library.theiet.org/content/journals/10.1049/mnl.2013.0352

[17] Y. Gotoh, K. Matsumoto, T. Maeda, E. B. Cooper, S. R. Manalis, H. Fang, S. C. Minne, T. Hunt, H. Dai, J. Harris, and C. F. Quate, "Experimental and theoretical results of room-temperature single-electron transistor formed by the atomic force microscope nano-oxidation process," *Journal of Vacuum Science & Technology A: Vacuum, Surfaces, and Films*, vol. 18, no. 4, pp. 1321–1325, 2000. [Online]. Available: http://avs.scitation.org/doi/10.1116/1.582347

[18] T. P. Burg, A. R. Mirza, N. Milovic, C. H. Tsau, G. A. Popescu, J. S. Foster, and S. R. Manalis, "Vacuum-packaged suspended microchannel resonant mass sensor for biomolecular detection," *Journal of Microelectromechanical Systems*, vol. 15, no. 6, pp. 1466–1476, 2006.

[19] A. Boisen and T. Thundat, "Design & fabrication of cantilever array biosensors," *Materials Today*, vol. 12, no. 9, pp. 32–38, 2009. [Online]. Available: http://dx.doi.org/10.1016/S1369-7021(09)70249-4

[20] C. A. Savran, S. M. Knudsen, A. D. Ellington, and S. R. Manalis, "Micromechanical detection of proteins using aptamer-based receptor molecules," *Analytical Chemistry*, vol. 76, no. 11, pp. 3194–3198, 2004.

[21] S. R. Manalis, E. B. Cooper, P. F. Indermuhle, P. Kernen, P. Wagner, D. G. Hafeman, S. C. Minne, and C. F. Quate, "Microvolume field-effect pH sensor for the scanning probe microscope," *Applied Physics Letters*, vol. 76, no. 8, pp. 1072–1074, 2000.

[22] N. C. Loh, M. A. Schmidt, and S. R. Manalis, "Sub-10 cm^3 interferometric accelerometer with nano-g resolution," *Journal of Microelectromechanical Systems*, vol. 11, no. 3, pp. 182–187, 2002.

[23] C. A. Savran, A. W. Sparks, J. Sihler, J. Li, W. C. Wu, D. E. Berlin, T. P. Burg, J. Fritz, M. A. Schmidt, and S. R. Manalis, "Fabrication and characterization of a micromechanical sensor for differential detection of nanoscale motions," *Journal of Microelectromechanical Systems*, vol. 11, no. 6, pp. 703–708, 2002.

[24] N. C. Loh, "High-Resolution Micromachined Interferometric Accelerometer," *Applied Physics Letters*, vol. 76, no. 22, pp. 3316–3318, 1992.

[25] H. B. Peng, C. W. Chang, S. Aloni, T. D. Yuzvinsky, and A. Zettl, "Ultrahigh frequency nanotube resonators," *Physical Review Letters*, vol. 97, no. 8, pp. 2–5, 2006.

[26] R. Datar, S. Kim, S. Jeon, P. Hesketh, S. Manalis, A. Boisen, and T. Thundat, "Cantilever sensors: Nanomechanical tools for diagnostics," *MRS Bulletin*, vol. 34, no. 6, pp. 449–454, 2009.

[27] B. Ilic, Y. Yang, and H. Craighead, "Virus detection using nanoelectromechanical devices," *Applied physics letters*, vol. 85, no. 13, pp. 2604–2606, 2004.

[28] S. M. Knudsen, M. G. Von Muhlen, D. B. Schauer, and S. R. Manalis, "Determination of bacterial antibiotic resistance based on osmotic shock response," *Analytical Chemistry*, vol. 81, no. 16, pp. 7087–7090, 2009.

[29] M. Godin, F. F. Delgado, S. Son, W. H. Grover, A. K. Bryan, A. Tzur, P. Jorgensen, K. Payer, A. D. Grossman, M. W. Kirschner, and S. R. Manalis, "Using buoyant mass to measure the growth of single cells," *Nature Methods*, vol. 7, no. 5, pp. 387–390, 2010. [Online]. Available: http://dx.doi.org/10.1038/nmeth.1452

[30] M. M. Stevens, C. L. Maire, N. Chou, M. A. Murakami, D. S. Knoff, Y. Kikuchi, R. J. Kimmerling, H. Liu, S. Haidar, N. L. Calistri, N. Cermak, S. Olcum, N. A. Cordero, A. Idbaih, P. Y. Wen, D. M. Weinstock, K. L. Ligon, and S. R. Manalis, "Drug sensitivity of single cancer cells is predicted by changes in mass accumulation rate," *Nature Biotechnology*, vol. 34, no. 11, pp. 1161–1167, 2016.

[31] J. Lee, R. Chunara, W. Shen, K. Payer, K. Babcock, T. P. Burg, and S. R. Manalis, "Suspended microchannel resonators with piezoresistive sensors," *Lab on a Chip*, vol. 11, no. 4, pp. 645–651, 2011.

[32] A. D. Pastina, D. Maillard, and L. G. Villanueva, "Microelectronic Engineering Fabrication of suspended microchannel resonators with integrated piezoelectric transduction," *Microelectronic Engineering*, vol. 192, pp. 83–87, 2018. [Online]. Available: https://doi.org/10.1016/j.mee.2018.02.011

[33] A. E. Cetin, M. M. Stevens, N. L. Calistri, M. Fulciniti, S. Olcum, R. J. Kimmerling, N. C. Munshi, and S. R. Manalis, "Determining therapeutic susceptibility in multiple myeloma by single-cell mass accumulation," *Nature Communications*, vol. 8, no. 1, 2017. [Online]. Available: http://dx.doi.org/10.1038/s41467-017-01593-2

[34] Y. Weng, F. F. Delgado, S. Son, T. P. Burg, S. C. Wasserman, and S. R. Manalis, "Mass sensors with mechanical traps for weighing single cells in different fluids," *Lab on a Chip*, vol. 11, no. 24, pp. 4174–4180, 2011.

[35] R. Chunara, M. Godin, S. M. Knudsen, and S. R. Manalis, "Mass-based readout for agglutination assays," *Applied Physics Letters*, vol. 91, no. 19, pp. 9–11, 2007.

[36] M. Godin, A. K. Bryan, T. P. Burg, K. Babcock, and S. R. Manalis, "Measuring the mass, density, and size of particles and cells using a suspended microchannel resonator," *Applied Physics Letters*, vol. 91, no. 12, pp. 17–19, 2007.

[37] S. Son, J. H. Kang, S. Oh, M. W. Kirschner, T. J. Mitchison, and S. Manalis, "Resonant microchannel volume and mass measurements show that suspended cells swell during mitosis," *Journal of Cell Biology*, vol. 211, no. 4, pp. 757–763, 2015.

[38] S. Byun, S. Son, D. Amodei, N. Cermak, J. Shaw, J. H. Kang, V. C. Hecht, M. M. Winslow, T. Jacks, P. Mallick, and S. R. Manalis, "Characterizing deformability and surface friction of cancer cells," *Proceedings of the National Academy of Sciences*, vol. 110, no. 19, pp. 7580–7585, 2013. [Online]. Available: http://www.pnas.org/cgi/doi/10.1073/pnas.1218806110

[39] J. Shaw Bagnall, S. Byun, D. T. Miyamoto, J. H. Kang, S. Maheswaran, S. L. Stott, M. Toner, and S. R. Manalis, "Deformability-based cell selection with downstream immunofluorescence analysis," *Integrative Biology (United Kingdom)*, vol. 8, no. 5, pp. 654–664, 2016. [Online]. Available: http://dx.doi.org/10.1039/C5IB00284B

[40] N. Cermak, S. Olcum, F. F. Delgado, S. C. Wasserman, K. R. Payer, M. A. Murakami, S. M. Knudsen, R. J. Kimmerling, M. M. Stevens, Y. Kikuchi, A. Sandikci, M. Ogawa, V. Agache, F. Baléras, D. M. Weinstock, and S. R. Manalis, "High-throughput measurement of single-cell growth rates using serial microfluidic mass sensor arrays," *Nature Biotechnology*, vol. 34, no. 10, pp. 1052–1059, 2016.

[41] J. Lee, W. Shen, K. Payer, T. P. Burg, and S. R. Manalis, "Toward attogram mass measurements in solution with suspended nanochannel resonators," *Nano Letters*, vol. 10, no. 7, pp. 2537–2542, 2010.

[42] A. Labuda, T. Brastaviceanu, I. Pavlov, W. Paul, and D. Rassier, "Optical detection system for probing cantilever deflections parallel to a sample surface," *Review of scientific instruments*, vol. 82, no. 1, p. 013701, 2011.

[43] O. Marti, A. Ruf, M. Hipp, H. Bielefeldt, J. Colchero, and J. Mlynek, "Mechanical and thermal effects of laser irradiation on force microscope cantilevers," *Ultramicroscopy*, vol. 42, pp. 345–350, 1992.

[44] H. Sadeghian, C.-K. Yang, K. B. Gavan, J. F. Goosen, E. W. van der Drift, H. S. van der Zant, A. Bossche, P. J. French, and F. van Keulen, "Some considerations of effects-induced errors in resonant cantilevers with the laser deflection method," *Journal of Micromechanics and Microengineering*, vol. 20, no. 10, p. 105027, 2010.

[45] T. Larsen, S. Schmid, S. Dohn, J. E. Sader, A. Boisen, and L. G. Villanueva, "Position and mode dependent optical detection back-action in cantilever beam resonators," *Journal of Micromechanics and Microengineering*, vol. 27, no. 3, 2017.

[46] M. J. Lachut and J. E. Sader, "Effect of surface stress on the stiffness of cantilever plates," *Physical review letters*, vol. 99, no. 20, p. 206102, 2007.

[47] J. Namchul and J. Sangmin, "Nanomechanical thermal analysis with silicon cantilevers of the mechanical properties of poly(vinyl acetate) near the glass transition temperature," *Macromolecules*, vol. 41, no. 24, pp. 9819–9822, 2008.

[48] F. Shen, P. Lu, S. O'Shea, K. Lee, and T. Ng, "Thermal effects on coated resonant microcantilevers," *Sensors and Actuators A: Physical*, vol. 95, no. 1, pp. 17–23, 2001.

[49] T. Remtema and L. Lin, "Active frequency tuning for micro resonators by localized thermal stressing effects," *Sensors and Actuators, A: Physical*, vol. 90, no. 3, pp. 326–332, 2001.

[50] "Allan variance: Noise analysis for gyroscopes," http://cache.freescale.com/files/sensors/doc/app_note/AN5087.pdf.

[51] M. Matejček and M. Šostronek, "New experience with allan variance: Noise analysis of accelerometers," in *2017 Communication and Information Technologies (KIT)*. IEEE, 2017, pp. 1–4.